Generative data-physics fusion for hierarchical reliability assessment

Lu-Kai Song[a], Matthias G.R. Faes[b], Fei Tao[c,d]*

[a] School of Mechanical Engineering, University of Science and Technology Beijing, Beijing 100083, China

[b] Chair for Reliability Engineering, TU Dortmund University, Dortmund 44227, Germany

[c] Digital Twin International Research Center, International Institute for Interdisciplinary and Frontiers, Beihang University, Beijing 100191, China

[d] School of Automation Science and Electrical Engineering, Beihang University, Beijing 100191, China

Abstract: Complex structural systems often exhibit hierarchical multi-site responses, interacting failure modes, and heterogeneous physical mechanisms, which challenge the construction of probabilistic models under limited data. Existing surrogate-based reliability methods predominantly rely on pointwise regression and simplified independence assumptions, leading to inaccurate tail characterization and insufficient modeling of cross-site and cross-mode dependencies. This study develops a generative data-physics (GenDP) fusion framework that integrates an outer-layer physics-data hierarchical collaboration and an inner-layer generative data-physics fusion mechanism. Herein, physical consistency conditions are embedded into Transformer, Diffusion and variational autoencoders type generative models to approximate physically consistent conditional distributions under limited data, while a physics-constrained conditional sampling strategy and Copula dependency reconstruction further enable hierarchical-to-system reliability propagation with realistic dependency representation. An aeroengine compressor blade-disc system is regarded as a case to demonstrate the effectiveness of the proposed method. Results show that the representative Diffusion-based Model with physics-informed enhancement (DFM-II) maintains reliability calculation accuracy above 97% under small-sample conditions, achieves a computational speed-up of approximately 138×-168× compared with direct Monte Carlo simulation, and exhibits strong robustness across varying sample sizes, with system-level accuracy variation confined within 2% (e.g., 96%-98%). Methods comparison reveal that the proposed GenDP fusion framework provides a scalable, physically coherent, and dependency-sensitive pathway for reliability assessment of complex hierarchical structural systems.

Keywords: generative model; data-physics; physics-informed; reliability; surrogate

* Corresponding author: ftao@buaa.edu.cn (F. Tao)

1. Introduction

Modern engineered systems such as aeroengine compressors, turbine stages, and wind turbine rotors increasingly operate under coupled multi-physics loading environments that combine aerodynamic, thermal, and structural effects [1-3]. Components located at different sites of a system, for example blade roots, disc cores, and casing interfaces, often experience similar boundary conditions but distinct local stress and strain states. These conditions induce multiple interacting failure mechanisms, including low-cycle fatigue, high-cycle fatigue, creep, and combined-cycle damage [4-5]. As a result, failures at one site or in one mode rarely occur in isolation. Instead, they propagate through correlated responses and shared load paths across the system [6-7]. In such settings, the reliability of a single site or a single failure mode no longer provides a sufficient description of structural safety. A hierarchical perspective that respects the physical organization of sites, modes, responses, and lifetimes becomes essential for realistic reliability evaluation.

High-fidelity physics-based models [8-9] provide important insight into these complex behaviors. Combined fluid and structural simulations can resolve local stress and strain fields at critical locations and can link operating parameters to lifetime responses [10-12]. However, these models are computationally expensive and the number of feasible simulations is often severely limited. In fact, uncertainties in loads parameters [13-15], material properties [16-18], and life model parameters [19-21] induce stochastic variability in structural responses and fatigue lifetimes, thereby making accurate reliability assessment challenging. These sources of uncertainty have been extensively studied within the framework of uncertainty quantification, and a variety of modeling and propagation techniques have been developed to characterize their effects. For example, through physics-informed Gaussian process modeling and convolutional dimension-reduction techniques [22-23]. Although their reliable propagation through high-fidelity physics-based models remains computationally prohibitive, rendering even widely used methods such as direct Monte Carlo simulation [24-26] impractical in this context. Analytical or semi-analytical reliability methods can reduce cost, but they usually require strong assumptions on the limit state function, probability distributions, or linearization around nominal conditions [27-29]. These simplifications may not hold for multi-site, multi-mode systems where responses exhibit strong nonlinearities and non-Gaussian traits. Surrogate modeling [30-32] has therefore become a widely used strategy to alleviate computational cost in reliability analysis. Polynomial chaos expansions [33-35], Kriging [36-38], Gaussian processes [39-41], support vector regression [42-44], and artificial neural network [45-47] based regressors can approximate the mapping from uncertain inputs to responses or lifetimes with significantly reduced computational effort. Most of these approaches, however, are designed as pointwise regression models. They focus on predicting mean responses or deterministic outputs at given input realizations [48-49]. In reliability evaluation, the tails of the response

or lifetime distributions often dominate failure probabilities. Pointwise surrogates can approximate central tendencies but may fail to capture the detailed distributional shapes, tail behavior, and cross-response correlations required for accurate failure probability estimation. In many existing studies, independence assumptions are further imposed between sites or modes to simplify modeling, which tends to underestimate failure probabilities in dependent systems.

Recent developments in physics-informed [50-51] and modular surrogate modeling [52-53] attempt to address some of these limitations. Physics-informed surrogates embed physical knowledge in different ways, for example through physics-based loss functions [54], physics-augmented training data [55], or physics driven model architectures [56]. These designs improve consistency with underlying mechanics and enhance interpretability, particularly when data are sparse. Modular or hierarchical modeling frameworks decompose complex systems into sub-modules and then aggregate their outputs to obtain system level quantities. Such strategies align with the physical structure of many engineering systems and improve scalability, in contrast to hierarchical Markov reliability modeling, which relies on discrete state transitions under the Markovian assumption. Despite these advances, most existing methods still operate at one of two levels only. They either focus on adding physical constraints at the surrogate level without reorganizing the system into a physically meaningful hierarchy, or they construct modular architectures while still relying on conventional regression type surrogates inside each module. In both cases, the treatment of multi-site and multi-mode dependency remains limited and the surrogate outputs mostly retain a deterministic character, in the sense that for a given input realization, the model produces a single point estimate (typically corresponding to the conditional mean or a most-likely response). However, deterministic point estimates are inherently insufficient for reliability analysis, where failure probabilities are dominated by the tails of response and lifetime distributions rather than their mean behavior. To overcome the limitations of deterministic point estimates, generative models such as transformer [57-58], diffusion [59-60] and variational autoencoders [61-62] offer an intrinsic capability to learn conditional probability distributions rather than deterministic mappings. By directly modeling distributions, generative models enable explicit representation of joint response distributions, complex tail behaviors, and interdependencies among multiple responses, providing a probabilistic modeling paradigm that is fundamentally more suitable for reliability analysis. However, standard deep generative models introduce new challenges when applied to engineering reliability problems. These models are typically data-hungry and prone to overfitting when trained on the limited datasets characteristic of high-fidelity simulations. Moreover, unconstrained generative models may generate physically infeasible samples, and their large hyperparameter spaces can lead to unstable training under small-sample conditions. Consequently, current applications of generative models require careful integration of physical guidance and stabilization mechanisms to ensure robustness and physical consistency. Consequently, current applications of generative models in reliability analysis are still scarce.

Existing attempts mostly treat them as black-box data generators and rarely integrate them with physical constraints, hierarchical system structure, or dependency modeling in a coherent reliability framework.

To the best of the authors' knowledge, three critical challenges remain open for hierarchical reliability assessment of dependent systems under limited data: (1) **Lacking a unified framework for hierarchical response-lifetime reconstruction:** existing studies, including independent surrogate modeling, global surrogate modeling, either fail to capture the dependency relationships among multiple failure modes and sites or cannot simultaneously satisfy accuracy and efficiency requirements. (2) **Failing to enforce physical knowledge in probabilistic predictions:** current surrogate and generative models typically constrain only pointwise outputs, making it difficult to guarantee physically plausible responses & lifetimes and often resulting in frequent and sometimes severe violations of stress limits, lifetime trends, and fatigue relationships. (3) **Missing a systematic mechanism for dependency-aware propagation:** existing approaches cannot reliably propagate physics-constrained generative outputs across sites and modes, leading to biased or overly optimistic system-level reliability estimates when nonlinear dependencies are strong.

To address these challenges, this study develops a generative data-physics (GenDP) fusion framework for hierarchical reliability assessment of dependent systems. The framework couples physics-based hierarchical decomposition with physics-informed generative distribution modeling in a consistent manner. At the hierarchical level, the system is decomposed into sites, failure modes, response quantities, and lifetime measures. This decomposition formulates the modeling tasks into physically interpretable units and clarifies how multi-site and multi-mode lifetimes should be assembled. At the surrogate level, generative models are trained to learn the full conditional distributions of responses and lifetimes given uncertain inputs, while hybrid data-physics loss functions enforce stress limits, monotonic trends, and so forth. A physics consistent conditional sampling strategy concentrates generated samples in physically admissible and near-failure regions, and a Copula based dependency model reconstructs cross-site and cross-mode dependence at the system level. The proposed GenDP fusion framework is demonstrated on a multi-site aeroengine compressor blade-disc system. The case study shows that the framework yields stable distribution modeling under limited data, reproduces dependency structures across blade root and disc core sites, and produces hierarchical and system reliability estimates that are consistent with physical expectations. Comparative results against classical regression surrogates confirm improvements in both distribution fidelity and computational efficiency.

The main novelty and contributions of this paper can be summarized in three aspects: (i) a physics hierarchical reliability framework is established, in which multi-site, multi-mode failure processes are represented through a layered structure linking inputs, responses, and lifetimes. This framework enables consideration of dependency relationships among different failure modes and failure sites, and enables reliability assessment for each failure mode and each

failure site of complex systems. (ii) a physics-informed generative surrogate modeling approach is proposed. Transformer, Diffusion, or VAE type generative models are trained under hybrid data-physics losses and physics consistent sampling, so that the learned conditional distributions and the generated samples satisfy mechanical admissibility, fatigue relationships, and near-failure emphasis even when only small simulation datasets are available. (iii) a dependency aware hierarchical to system reliability propagation scheme is developed. Furtherly, the large batches of physics consistent generative samples are combined with Copula dependency reconstruction to obtain component level and system level failure probabilities that account for nonlinear cross-site and cross-mode correlations.

The remainder of this paper is organized as follows. Section 2 introduces the generative data-physics fusion concept and presents the mathematical formulations. Section 3 establishes the GenDP-based hierarchical reliability framework. Section 4 establishes the GenDP models for an aeroengine compressor. Section 5 presents dependent reliability & sensitivity evaluation, and method comparisons. Section 6 summarizes the main findings of this study.

2. Generative data-physics fusion approach

This section elaborates on the generative data-physics fusion approach, encompassing the concept, and mathematical derivations of physics-dominated outer fusion and data-dominated inner fusion.

2.1. Generative data-physics fusion concept

Reliability assessment of multi-site, multi-mode structural systems exhibits the complex characteristics of hierarchical physical structures and probabilistic modeling, particularly when simulation and/or experiment data are limited. To address this problem, a generative data-physics (GenDP) fusion concept is proposed in this paper. As illustrated in **Fig. 1**, the GenDP fusion concept presents a dual-layer mechanism that tightly couples physics-based hierarchical decomposition (outer layer) and data-informed generative modeling (inner layer). The framework thereby forms a unified, structured pathway from physical modeling to reliability evaluation.

The GenDP fusion concept relies on two interacting layers. The outer layer establishes the physical structure. Here, the engineering system is decomposed into units, subsystems, and the overall system, according to realistic load transfer paths, spatial dependencies, and failure-mode distinctions. This hierarchy sets clear boundaries for modeling tasks and dictates how responses and lifetimes propagate through different structural levels. As a result, the outer layer provides a physics-based organizational backbone that constrains and guides the modeling process. The inner layer complements this physical structure by introducing generative modeling methods, such as Transformer, Diffusion, or Variational Autoencoder (VAE). These methods learn conditional probability distributions of structural responses and lifetimes. In contrast to conventional surrogate models, the GenDP models explicitly embed physics-informed

constraints. These constraints include stress admissibility, fatigue-life monotonicity, and structural feasibility. The inner layer thus captures probabilistic uncertainty and tail behavior in a manner consistent with physical principles. Rather than purely data-driven predictions, the inner layer achieves data-physics fusion informed by explicit physical requirements. Crucially, the outer and inner layers do not operate separately but interact continuously in a feedback loop. The physical decomposition in the outer layer directly shapes the generative distributions learned by the inner layer. Conversely, the generative distributions produced by the inner layer inform the outer layer's reliability and sensitivity analyses. This dual-direction interaction is the essence of GenDP fusion. It ensures physically consistent reconstruction of response and lifetime distributions, even when data availability is limited. This integrated generative data-physics fusion concept can be summarized by, i.e.,

$$\underbrace{\mathcal{F}_{\text{phys}} : \text{System} \to \{\text{Subsystems}\} \to \{\text{Units}\}}_{\text{physics-dominated outer fusion}} \Rightarrow \underbrace{\mathcal{M}_{\text{gen}} : x \mapsto p(y \mid x, \theta_{\text{phys}})}_{\text{data-dominated inner fusion (GenAI)}} \Rightarrow \underbrace{\mathcal{R}_{\text{hier}} = \mathbb{P}(g_{s,m}(x) > 0)}_{\text{hierarchical reliability evaluation}} \quad (1)$$

The GenDP approach is thus distinct from traditional surrogate methods, as it does not simply impose physics as penalty terms or rely solely on statistical inference. Instead, GenDP aligns modeling structures with physical hierarchies and simultaneously expands uncertainty modeling capabilities. This integrated concept provides the theoretical foundation for the mathematical formulations and the computational strategies in Section 2.2.

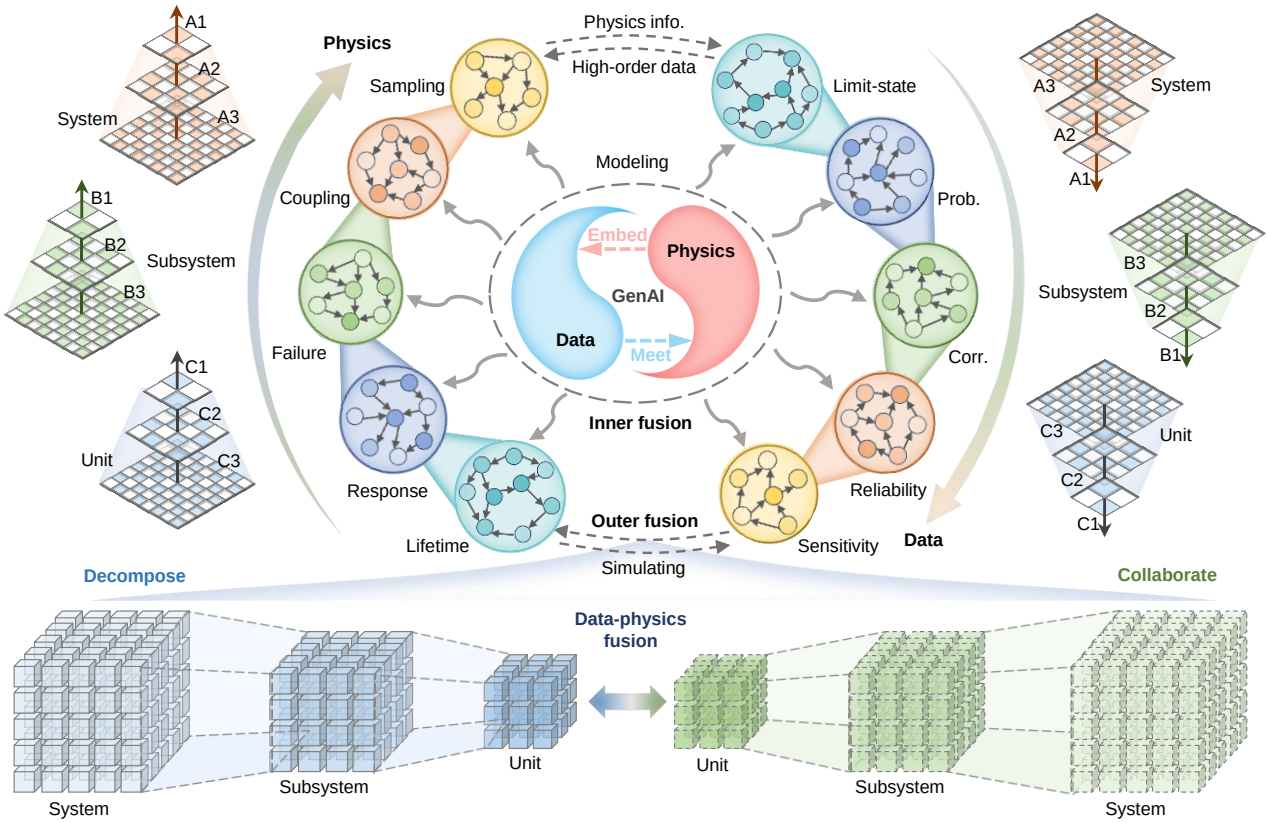

Fig. 1 The generative data-physics fusion concept

2.2. Mathematical derivations of GenDP approach

The mathematical formulation of the proposed generative data-physics (GenDP) fusion approach integrates hierarchical physical modeling, small-batch simulations, and generative surrogate modeling into a unified framework, as illustrated in **Fig. 2**. The method establishes a coherent mathematical pipeline connecting input uncertainties with multi-site fatigue responses and lifetimes. Initially, a set of multidimensional inputs propagates through coupled stress-strain relations and damage mechanisms, resulting in multi-mode fatigue responses and lifetimes at critical structural sites. This physics-based forward process defines fundamental structural relationships that the generative surrogate must accurately represent. Upon obtaining the small-batch dataset, modeling progresses through three coupled stages: physics-informed conditional sampling, generative modeling with hybrid data-physics losses, and Bayesian optimization for surrogate hyperparameter tuning. Specifically, the conditional sampling stage incorporates feasibility conditions, emphasizes near-failure scenarios, and leverages uncertainty-based sampling to create an informative data subset. In the generative modeling stage, the Transformer, Diffusion, or VAE architectures approximate the full conditional distributions of structural responses and lifetimes, embedding physical constraints such as admissible stress thresholds, fatigue monotonicity conditions, and structural feasibility criteria. To ensure robust training, Bayesian optimization adaptively selects optimal hyperparameters, enhancing the generative model's stability and predictive accuracy. Together, these procedures constitute the inner layer of GenDP, in which data-driven distribution modeling is consistently shaped by hierarchical physical constraints.

The resulting generative surrogate produces large-scale sample sets, facilitating probabilistic characterization and correlation quantification across structural sites and fatigue modes. These generative outputs subsequently support the structured reliability assessment and sensitivity analysis. In sum, this methodological framework can be detailed through two main complementary aspects: (i) the outer-layer physics-data hierarchical collaboration (Section 2.2.1), and (ii) the inner-layer generative data-physics fusion mechanism (Section 2.2.2).

2.2.1. Physics-dominated outer data-physics fusion

The outer layer of the GenDP fusion framework defines the physics-dominated pathway through which uncertainties in the inputs propagate to multi-site and multi-mode fatigue lifetimes. As illustrated in **Fig. 2**, this layer contains two structurally consistent streams: a forward physics-based propagation, which provides a small but reliable dataset derived from thermo-mechanical simulations, and a probabilistic reconstruction stream where the trained generative model produces large-scale samples consistent with the original physical mapping. The coherence between these two streams ensures that generative modeling strictly follows the hierarchical physical structure of the system.

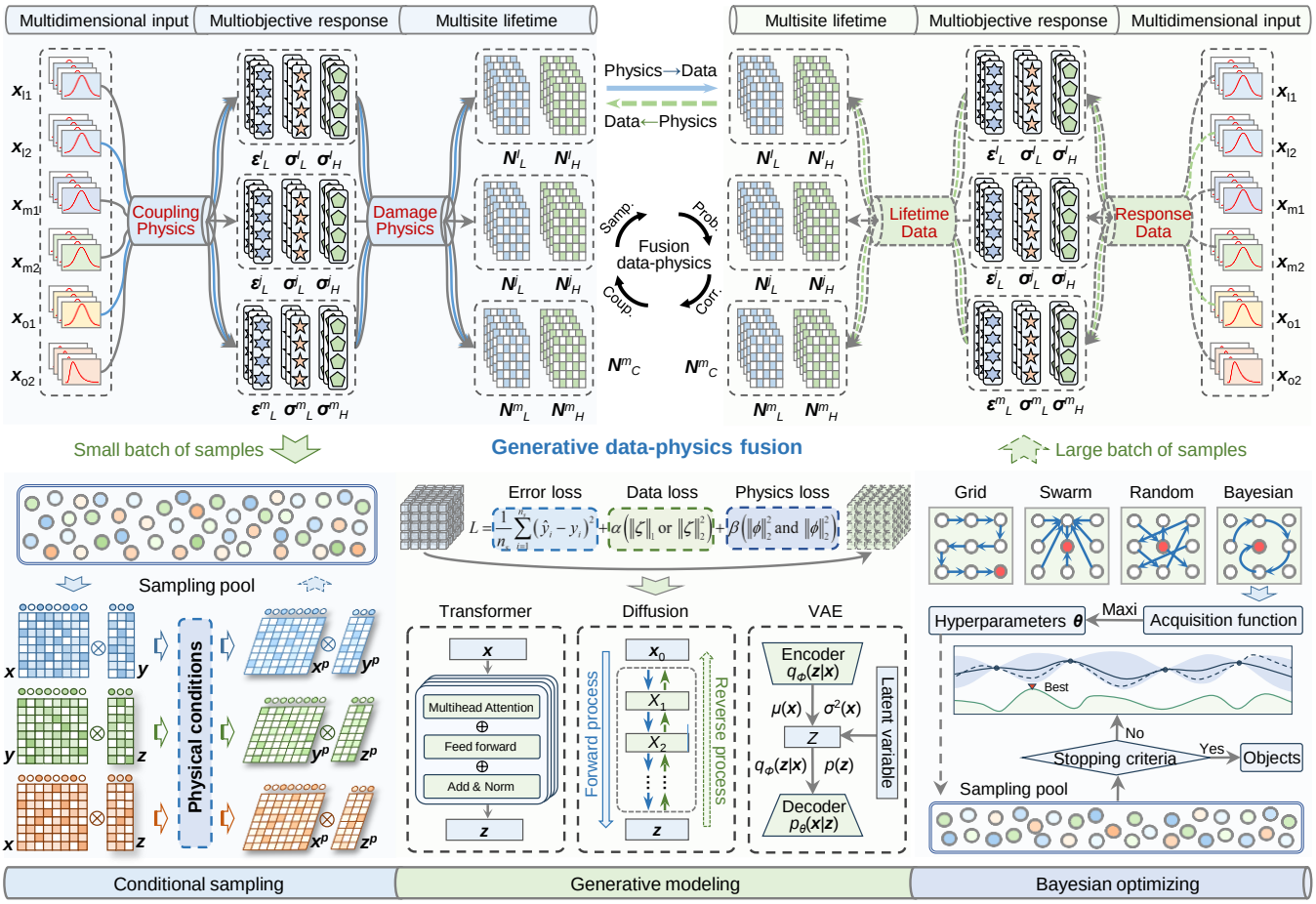

Fig. 2 Mathematical modeling streamline of generative data-physics fusion

(1) Physics-dominated single-sample propagation

For a given realization of uncertain inputs, the forward mapping begins with

$$\boldsymbol{x} = (x_{l1},\ x_{l2},\ x_{m1},\ x_{m2},\ x_{o1},\ x_{o2})^{\mathrm{T}} \tag{2}$$

where x_{l1}, x_{l2} denote the load-type inputs; x_{m1}, x_{m2} the material-type inputs; x_{o1}, x_{o2} the fatigue-model inputs.

For any realization of inputs, the physics-based response operator evaluates the each-site each-mode responses:

$$\boldsymbol{y}_{s,\,m}^{resp} = T_{s,\,m}^{resp}(\boldsymbol{x}),\ m \in \{\mathrm{LCF}, \mathrm{HCF}, \mathrm{CCF}\} \tag{3}$$

where $y_{s,\,m}^{resp}$ indicates the strain-stress response at site s, mode m; $T_{s,\,m}^{resp}(\bullet)$ denotes the physics-based operator that maps the input vector $\boldsymbol{x}$ to the corresponding site-mode response.

The fatigue damage index for each site-mode pair $D_{s,m}$ is expressed as

$$D_{s,m} = h_{s,m}(y_{s,\,m}),\quad N_{s,m} = g_{s,m}(D_{s,m},\ \boldsymbol{x}) \tag{4}$$

where $h_{\mathrm{s,m}}(\cdot)$ indicates the fatigue damage operator depending on material fatigue parameters; $N_{\mathrm{s,m}}$ the lifetime at site s, mode m; $g_{\mathrm{s,m}}(\cdot)$ the general LCF/HCF/CCF operator that incorporates strain-based, stress-based, and mode-dependent fatigue mechanisms. The overall physics-based propagation can thus be summarized compactly as

$$\boldsymbol{x} \xrightarrow{T_{s,m}^{resp}} \boldsymbol{y}_{s,m}^{resp} \xrightarrow{h_{s,m}} D_{s,m} \xrightarrow{g_{s,m}} \{N_{s,m}^{phys}\} \tag{5}$$

where $\{ N_{s,m}^{phys} \}$ denotes the lifetimes computed entirely from physics-based models.

Based on these physics-consistent samples, the inner-layer fusion mechanism introduced in Section 2.2.2 can train the generative surrogate model that captures the underlying physical relationships and extends them to large-scale probabilistic sampling. This enables the distribution-level amplification of multi-site responses and lifetimes while preserving the hierarchical physical structural characteristics.

(2) Data-dominated large-sample propagation

Once the generative surrogate has learned the physics-derived mapping, the distributional form of the responses and lifetimes is obtained as

$$\boldsymbol{y}_{s,m}^{resp,(j)} \sim p_\theta\left(\boldsymbol{y}_{s,m}^{resp} \middle| \boldsymbol{x}^{(j)}\right), N_{s,m}^{(j)} \sim p_\theta\left(N_{s,m} \middle| \boldsymbol{y}_{s,m}^{resp,(j)}, \boldsymbol{x}^{(j)}\right) \tag{6}$$

where $p_\theta(\boldsymbol{y}|\boldsymbol{x})$ denotes generative model-based conditional distribution of responses; $p_\theta(N|\boldsymbol{y}, \boldsymbol{x})$ the conditional lifetime distribution. For data-dominated large-sample propagation, independent samples are generated by repeating (6) for j=1, …, M with $M \gg n$, and n is the training sample size.

The corresponding large-batch propagation can be written as

$$\boldsymbol{x}^{(j)} \xrightarrow{p_\theta(\boldsymbol{y}|\boldsymbol{x})} \boldsymbol{y}^{resp,(j)} \xrightarrow{p_\theta(N|\boldsymbol{y},\boldsymbol{x})} N_{s,m}^{(j)} \tag{7}$$

The built propagation ensuring that the large-sample outputs inherit the structure of the underlying physics mapping while providing scalable distributions for subsequent hierarchical reliability assessment.

2.2.2. Data-dominated inner data-physics fusion

The inner layer of the GenDP fusion framework formulates how physics-informed constraints, data-driven generative modeling, and adaptive hyperparameter optimization interact to construct distribution-consistent surrogates under limited data. This layer contains three tightly connected components: conditional sampling, generative modeling with hybrid data-physics losses, and Bayesian optimization, ensuring that the generative surrogate maintains physical consistency while amplifying the small-batch physics-derived samples into large-scale probabilistic datasets.

(1) Physics-consistent conditional sampling

To construct an informative sampling pool from the initial distribution $p_0(x)$, the physics-driven constraints are introduced. The conditional sampling density is formulated as

$$p_{cond}(\boldsymbol{x}) \propto p_0(\boldsymbol{x})\ \mathbf{1}_{C_{phys}}(\boldsymbol{x}) w_{nf}(\boldsymbol{x}) w_{uq}(\boldsymbol{x}) \tag{8}$$

where $p_0(\boldsymbol{x})$ indicates the baseline input distribution; C_{phys} the physical feasibility domain; $w_{nf}(\boldsymbol{x})$ the near-failure weight; $w_{uq}(\boldsymbol{x})$ the model-based uncertainty weight. Herein, $\mathbf{1}_{C_{phys}}(\boldsymbol{x})$ enforces physical admissibility with respect to stress limits, material bounds, and feasible operating conditions; $w_{nf}(\boldsymbol{x})$ emphasizes samples close to the physics-evaluated limit-state surface; and $w_{uq}(\boldsymbol{x})$ promotes samples with high predictive uncertainty.

The near-failure weighting is defined through an exponential proximity rule, i.e.,

$$w_{nf}(\boldsymbol{x}) = \exp\left[-\beta \min_{s,m} \left| g_{s,m}^{\text{phys}}(\boldsymbol{x}) \right| \right] \quad w_{uq}(\boldsymbol{x}) = \sigma_{\theta 0}^2(\boldsymbol{x}) + \gamma H_{\theta 0}(\boldsymbol{x}) \tag{9}$$

where β denotes the near-failure sensitivity coefficient controlling the emphasis on low-margin regions; γ regulates the weighting of model-uncertainty measures; $g_{s,m}^{\text{phys}}(\boldsymbol{x})$ represents the physics-evaluated limit-state function; $\sigma_{\theta 0}^2(\boldsymbol{x})$ the predictive variance; $H_{\theta 0}(\boldsymbol{x})$ the entropy derived from an initial model with parameters θ_0. Here, β appears as the parameter that determines the steepness of the exponential proximity weighting.

The resulting conditional sampling pool takes the form as follows,

$$S = \left\{ \boldsymbol{x}^{(i)} \sim p_{cond}(\boldsymbol{x}) \mid i = 1, \ \ldots, \ n_{pool} \right\} \tag{10}$$

where S indicates the conditional sampling pool; n_{pool} the pool size. The built sampling pool is conducive to yielding a physically consistent and statistically enriched dataset for generative modeling.

(2) Generative modeling with hybrid data-physics losses

The generative model approximates the joint distribution of responses and lifetimes while incorporating physical constraints. The mapping is expressed by latent transformation, decoding, and lifetime reconstruction:

$$\boldsymbol{z} = f_\theta(\boldsymbol{x}, \varepsilon), \ \boldsymbol{y} = g_\theta(z, \boldsymbol{x}), \ N = k_\theta(\boldsymbol{y}, \boldsymbol{z}, \boldsymbol{x}) \tag{11}$$

where f_θ, g_θ, k_θ are the encoder, response decoder, and lifetime decoder, respectively; ε the latent noise; z the latent variable. The training is guided by hybrid loss combines data consistency, distribution alignment, and physics regularity

$$L(\theta) = L_{err} + \lambda_{dist} L_{dist} + \lambda_{phys} L_{phys} \tag{12}$$

where L_{err} ensures sample-wise agreement with the physics-derived dataset; L_{dist} aligns the generative distribution with empirical statistics through KL- or Wasserstein-type measures; and L_{phys} encodes the physical constraints required by the fatigue behaviour. Specifically, it incorporates allowable stress limits, enforces monotonic degradation of lifetime with respect to stress responses or rotational speed w, and ensures consistency with fatigue-law predictions. These constraints are expressed through the penalty terms Φ_σ, Φ_{mono}, and Φ_{life} in Eq. (13), which jointly enforce physical admissibility of the reconstructed responses and lifetimes.

$$L_{phys} = \eta_1 \Phi_\sigma + \eta_2 \Phi_{\text{mono}} + \eta_3 \Phi_{\text{life}} \tag{13}$$

where the three penalty components enforce allowable stress bounds, prohibit non-physical lifetime trends, and align reconstructed lifetimes with physics-based lifetime operators. The surrogate distribution is obtained by minimizing

$$\theta^* = \arg\min_{\theta} L(\theta) \tag{14}$$

where θ^* indicates the optimized generative model parameters, the obtained parameters ensuring that the learned distributions remain both statistically representative and physically admissible.

(3) Bayesian optimization for hyperparameter selection

Model hyperparameters θ (i.e., latent dimension, depth, noise schedule) are being searching through Bayesian optimization to enhance training stability and predictive accuracy

$$\theta^* = \arg\max_{\theta} a(\theta \mid D, S) \tag{15}$$

where D denotes the training dataset containing paired input-response samples; S represents the hyperparameter search space within which Bayesian optimization is performed; $a(\cdot)$ indicates an acquisition function, by incorporating the validation loss, lifetime-distribution variance, and physics-violation metrics, it can be represented by

$$a(\theta) = -L_{val}(\theta) - \omega_1 Var[N_\theta] - \omega_2 R_{\text{phys}}^{\text{val}}(\theta) \tag{16}$$

where $L_{val}(\theta)$ denotes the validation loss; $Var[N_\theta]$ the variance of generated lifetime; $R_{\text{phys}}^{\text{val}}$ the physics penalties on validation set; w_1, w_2 are non-negative weighting coefficient, so that hyperparameters with stronger physical and statistical performance receive higher scores. Hyperparameter updates proceed iteratively as

$$\theta_{t+1} = \theta_t + \Delta\theta(a(\theta_t)) \tag{17}$$

where θ_t is the hyperparameters at iteration t; $\Delta\theta(\cdot)$ the Bayesian optimization update step. It will proceed until convergence criteria are satisfied, thereby leading to a stable and physically aligned generative model.

3. Hierarchical reliability framework with GenDP fusion

The proposed hierarchical reliability framework establishes a structured pathway for propagating uncertainties from the physics-based decomposition of the system to distribution-level reliability evaluation. As shown in **Fig. 3**, the framework couples physical modeling with generative data expansion, enabling a consistent transition from limited small-batch simulations to large-scale probabilistic characterization. The seven steps form a coherent pipeline in which the physics-based hierarchy defines how information flows across structural levels, and the generative surrogate provides scalable uncertainty representations for reliability and sensitivity evaluation.

Step 1: Physical decomposition. The hierarchical system is decomposed into site, mode, and response levels, where each level corresponds to specific failure, damage, and coupling physics. This decomposition establishes physically interpretable modeling units and determines how site-mode responses and lifetimes are organized.

Step 2: Physical analysis. Coupled fluid, structural, and fatigue analyses are performed to generate physically reliable responses. The simulations provide stresses, strains, and initial lifetime quantities at critical locations, forming the mechanistic basis for subsequent data-driven modeling.

Step 3: Small batch of samples. A small-batch dataset is constructed by filtering original samples through physical feasibility conditions such as stress limits and material admissibility. This reduced pool captures the essential physics while preserving the variability required for learning.

Step 4: Generative modeling. Transformer-, diffusion-, and VAE-type generative surrogates are trained to approximate the conditional distributions of responses and lifetimes under the hybrid data-physics losses. The generative model reconstructs full probability distributions required for reliability estimation.

Step 5: Bayesian optimization. Hyperparameters controlling model depth, latent dimension, and noise schedules are selected using Bayesian optimization approach. The acquisition function in BO algorithm is promising to balance the data fidelity, distribution alignment, and physics-violation penalties.

Step 6: Large batch of samples. With optimized parameters, the generative surrogate model is used to produce a large batch of samples, enabling distribution reconstruction and correlation quantification across sites and modes.

Step 7: Hierarchical evaluation. The large-batch samples are propagated through the limit-state functions to evaluate the hierarchical reliability and the associated sensitivities. Here, the cross-site and cross-mode dependencies are reconstructed using a Copula representation, which provides the joint structure required for aggregating hierarchical failure events. This dependency-aware formulation enables the calculation of both hierarchical reliability R_{hier} with sensitivity $S_{\text{hier}}^{(k)}$ and system reliability R_{system} with sensitivity $S_{\text{sys}}^{(k)}$ via Eqs. (18-21). Hierarchical reliability is evaluated at the site/mode level, while system reliability refers to the aggregation over all sites and modes.

$$R_{\text{hier}} = \frac{1}{N}\sum_{i=1}^{N} I\left(g_{s,m}\left(x^{(i)}\right) > 0\right) \tag{18}$$

$$R_{\text{system}} = \frac{1}{N}\sum_{i=1}^{N} I\left(\min_{(s,m)} g_{s,m}\left(x^{(i)}\right) > 0\right) \tag{19}$$

$$S_{\text{hier}}^{(k)} = \frac{1}{N}\sum_{i=1}^{N} \delta\left(g_{s,m}\left(x^{(i)}\right)\right)\frac{\partial}{\partial x_k}\left(g_{s,m}\left(x^{(i)}\right)\right) \tag{20}$$

$$S_{\text{sys}}^{(k)} = \frac{1}{N}\sum_{i=1}^{N} \delta\left(\min_{s,m} g_{s,m}\left(x^{(i)}\right)\right)\frac{\partial}{\partial x_k}\left(\Phi_K\left(z_1(x^{(i)}),\ldots,z_K(x^{(i)});\Sigma\right)\right) \tag{21}$$

where $g_{s,m}(\cdot)$ denotes the site-mode limit-state function, with $g_{s,m}(\cdot)>0$ indicating secure state, and vice versa.

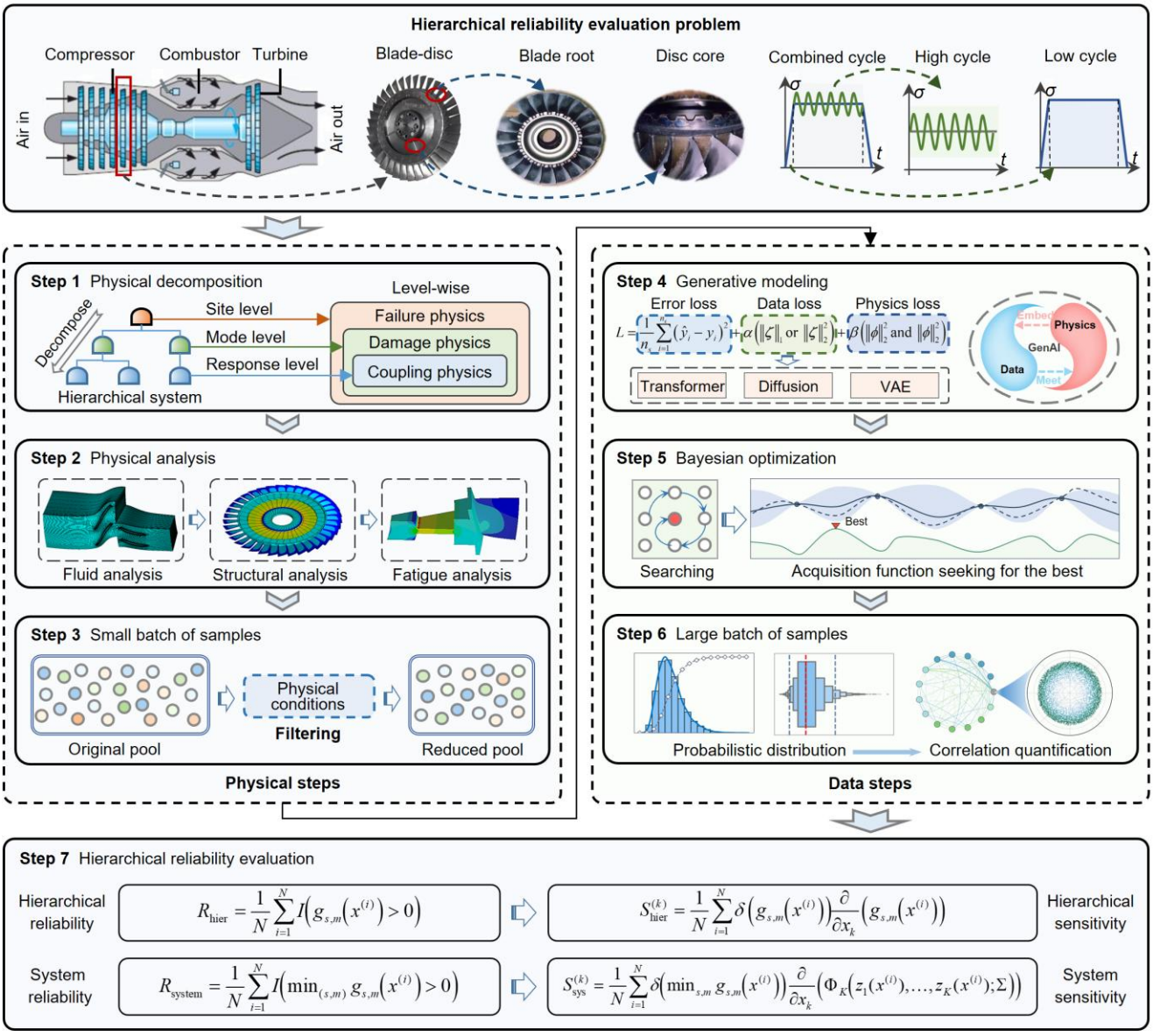

Fig. 3 Essential procedures of the hierarchical reliability framework

4. Generative modeling for aero-engine compressors

In this section, an aeroengine compressor exhibiting dependent composite-cycle failure characteristics is selected as a practical example to illustrate the capability and robustness of the developed generative data-physics fusion approach. The compressor consists of titanium superalloy [63-64] numerical experiments are conducted using a standard desktop computer configured with a 3.6 GHz Intel® Core™ i7-9700K processor and 16 GB of RAM.

4.1. Fluid-mechanic co-simulation

To generate physically reliable small-batch samples for the generative data-physics fusion framework, a coupled fluid-mechanic co-simulation is carried out for a representative compressor blade-disc sector. The analysis follows the typical aeroengine flow path, in which the upstream compressor region provides highly non-uniform aerodynamic loading to both rotor and stator components. As illustrated in **Fig. 4(a-b)**, a two-sector configuration containing one

rotor blade and one stator passage is extracted from the full annulus, enabling efficient computation while preserving the essential flow and structural features. The fluid domain is constructed using refined hexahedral meshes near the blade surfaces and the inter-row region, whereas the structural domain of the blade and disc is modeled using a cyclic-symmetry finite-element representation, as shown in **Fig. 4(e)**.

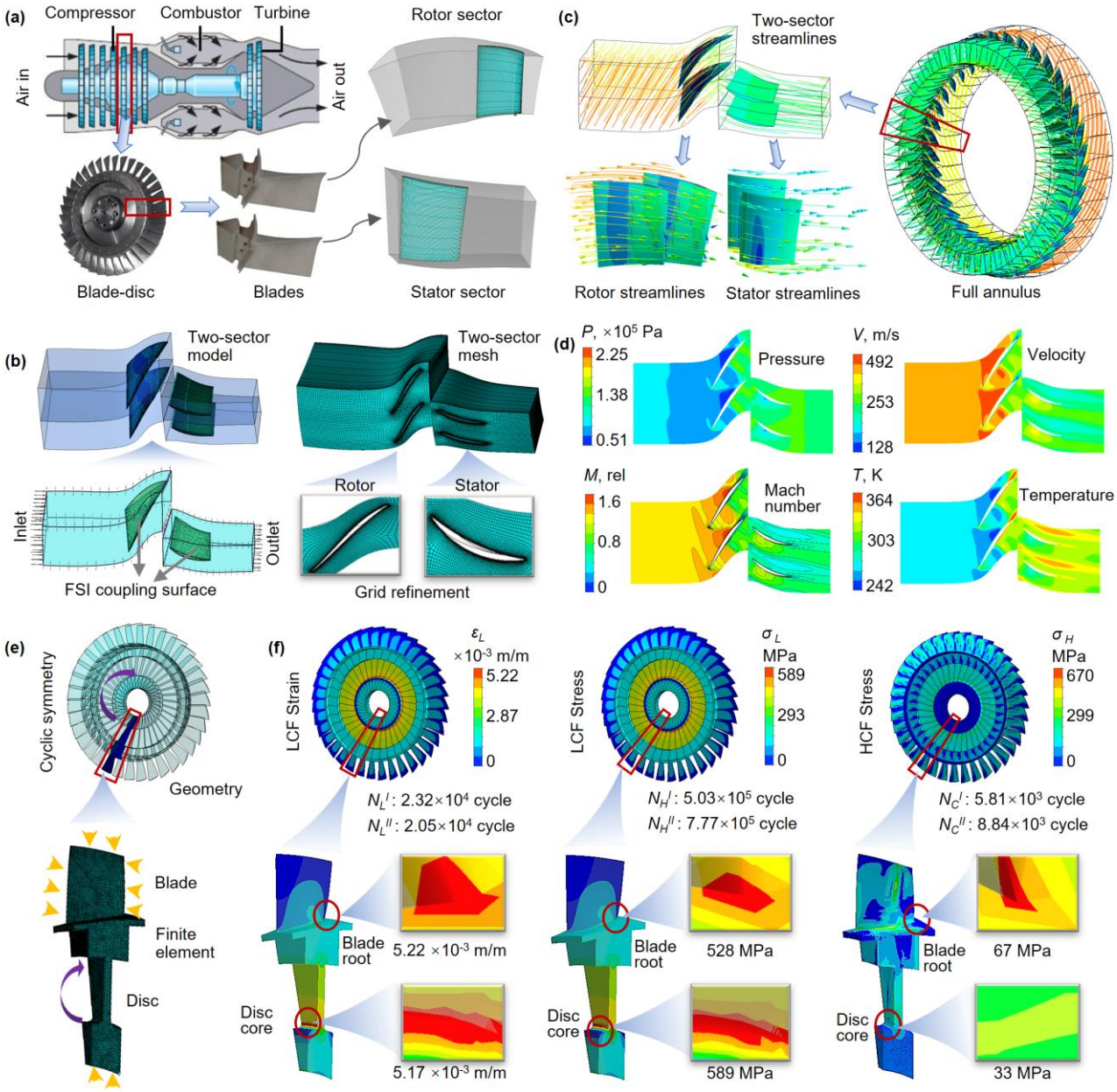

Fig. 4 Fluid dynamics and structural mechanics co-simulation for aeroengine compressor. (a) sketch of stator-rotor sectors; (b) Fluid meshing; (c) fluid streamlines; (d) fluid dynamic results; (e) structural meshing; (f) structural dynamic results

The aerodynamic field is resolved using steady RANS solutions, with the inlet total pressure and temperature prescribed based on representative compressor operating conditions. **Fig. 4(c-d)** show the resulting flow patterns, where the pressure ranges from approximately 0.5×10^5 to 2.25×10^5 Pa, and the local Mach number varies between 0 and 1.6 across the rotor-stator interface. Correspondingly, the flow velocity spans from 128 to 492 m/s, and the temperature distribution ranges from 242 to 364 K. These gradients produce spatially varying aerodynamic forces that are

transferred to the structural domain through a fluid structure interaction (FSI) coupling surface. The structural responses are evaluated under the mapped aerodynamic pressure, with cyclic-symmetry boundary conditions applied to represent the full annulus environment. The distributions of low-cycle fatigue (LCF) strain, LCF stress, and high-cycle fatigue (HCF) stress are shown in **Fig. 4(f)**. Herein, the LCF strain reaches 5.22×10^{-3} m/m at the blade root and 5.17×10^{-3} m/m at the disc core. The LCF stress attains 528 MPa at the blade root and 589 MPa in the disc core. For the HCF case, the stress level is 67 MPa at the blade root and 33 MPa at the disc core. The corresponding fatigue lifetimes are summarized as follows: the LCF lifetimes at site I and site II are approximately 2.32×10^{4} and 2.05×10^{4} cycles, the HCF lifetimes at site I and site II are approximately 5.03×10^{5} and 7.77×10^{5} cycles, and the combined-cycle fatigue (CCF) lifetimes at site I and site II are approximately 5.81×10^{3} and 8.84×10^{3} cycles. These lifetime values serve as physically grounded reference points for guiding the subsequent conditional sampling and dataset establishment.

4.2. Hierarchical dataset establishment

To support the proposed generative data-physics fusion framework, a hierarchical dataset was constructed with input uncertainties defined based on engineering material handbook [63-64] data for typical aeroengine materials, representative cruise operating conditions and FSI-derived boundary fluctuations, and published fatigue test statistics, to characterize the propagation of uncertainties from operating conditions, material properties, and fatigue parameters to multi-site responses and lifetimes. **Table 1** summarizes the statistical properties of the selected inputs, including aerodynamic and thermodynamic quantities (P_{I}, P_{O}, T), material parameters (ρ, E, μ, α), and rotational speed w. These variables follow Gaussian distributions reflecting realistic compressor variability; for example, P_{I} ranges from 0.967 to 1.048×10^{5} Pa with a standard deviation of 0.017×10^{5} Pa, and temperature spans 270.3-298.3 K with a mean of 287.1 K. The rotational speed fluctuates within -1978 to -1811 rad/s, the negative sign only indicates the direction of rotation and does not affect the calculation of stress amplitude and lifespan. Fatigue parameters were also included to represent material scatter, where the strength index b and ductility index c are modeled as Gaussian variables, while the coefficients σ_f' and ε_f' follow Gaussian and lognormal distributions, respectively. Before constructing the training subset, a two-stage physics-oriented filtering procedure was applied to remove samples that were physically inadmissible or numerically unstable. First, all inputs generated by Latin hypercube sampling (LHS) were screened using a feasibility domain C_{phys}, eliminating cases violating operational bounds such as $P_{\mathrm{I}}>1.05\times10^{5}$ Pa, $T>300$ K, or material constraints such as $E>120$ GPa and $\rho<4000$ kg/m^3. Second, after the fluid-structural simulations, a viability checks discarded samples exhibiting non-physical responses, including excessive LCF stresses (>650 MPa), unrealistically large LCF strains ($>7.0\times10^{-3}$ m/m). This physically consistent filtering ensured that the retained dataset captured feasible operating states and mechanically reliable responses.

The output space follows the hierarchical configuration of the blade-disc system. For each realization, LCF and HCF responses were recorded at site I (blade root) and site II (disc core). The LCF strain at site I varies between 4.71×10^{-3} m/m and 5.85×10^{-3} m/m, with stresses between 481-569 MPa, while site II responses fall within comparable intervals. HCF stresses reach up to 92.1 MPa at site I and 76.1 MPa at site II. Based on these responses, fatigue lifetimes were evaluated using standard LCF, HCF, and CCF formulations. The resulting lifetime variables follow lognormal distributions. At site I, the mean LCF lifetime is 3.116×10^4 cycles, with a standard deviation of 0.920×10^4 cycles; the corresponding HCF lifetime has a mean of 4.553×10^5 cycles and a standard deviation of 2.978×10^5 cycles, while the mean CCF lifetime is 0.543×10^4 cycles with a standard deviation of 0.298×10^4 cycles. At site II, the mean LCF lifetime is 2.700×10^4 cycles with a standard deviation of 0.777×10^4 cycles; the HCF lifetime has a mean of 1.076×10^6 cycles and a standard deviation of 1.281×10^6 cycles; and the mean CCF lifetime is 0.995×10^4 cycles with a standard deviation of 0.617×10^4 cycles. The resulting dataset forms a physically interpretable, hierarchically structured input-output space that underpins the subsequent generative modeling and reliability assessment.

Table 1 Statistical characteristics of input variables and output responses for compressor blade-disc

Variables	Symbol	Unit	Distribution	Min	Max	Mean	Std.	Kurtosis	Skewness
Inlet total pressure	P_I	10^5 Pa	Gaussian	0.967	1.048	1.013	0.017	-0.014	-0.339
Outlet pressure	P_O	10^5Pa	Gaussian	1.286	1.409	1.359	0.026	-0.364	-0.092
Regular velocity	v	rev/min	Gaussian	-18723	-17141	-18042	337.8	-0.034	0.363
Temperature	T	K	Gaussian	270.3	298.3	287.1	5.701	0.109	-0.261
Density	ρ	kg/m^3	Gaussian	4262	4597	4437	78.05	-0.593	-0.142
Young's Modulus	E	GPa	Gaussian	107	120	114	2.69	-0.118	-0.275
Poisson's Ratio	μ	-	Gaussian	0.330	0.360	0.343	0.006	0.317	0.249
Heat expansion	α	10^{-6} /°C	Gaussian	8.73	9.52	9.12	0.184	-0.711	0.097
Rotational speed	w	rad/s	Gaussian	-1978	-1811	-1885	34.15	-0.050	-0.046
Fatigue strength index	b	-	Gaussian	-0.147	-0.133	-0.140	0.003	0.048	0.295
Fatigue ductility index	c	-	Gaussian	-1.012	-0.910	-0.963	0.018	0.035	-0.029
Fatigue strength parameter	σ_f'	MPa	Gaussian	1644	1810	1724	36	-0.197	-0.137
Fatigue ductility parameter	ε_f'	-	Lognormal	1.074	1.177	1.125	0.021	0.296*	-0.166*
Ultimate Stress	σ_{lim}	MPa	Gaussian	926	1017	974	19.07	-0.180	0.020
LCF stress site I	σ_L^I	MPa	Gaussian	481	569	526	21.99	-0.780	0.024
LCF strain site I	ε_L^I	10^{-3} m/m	Gaussian	4.71	5.85	5.21	0.25	-0.513	0.255
HCF stress site I	σ_H^I	MPa	Gaussian	69.2	92.1	81.5	4.763	-0.167	-0.099
LCF stress site II	σ_L^{II}	MPa	Gaussian	535	634	587	24.71	-0.779	0.011
LCF strain site II	ε_L^{II}	10^{-3} m/m	Gaussian	4.71	5.80	5.17	0.25	-0.553	0.267
HCF stress site II	σ_H^{II}	MPa	Gaussian	54.4	76.1	66.2	4.618	-0.176	-0.429
LCF life site I	N_L^I	10^4 cycles	Lognormal	1.514	5.856	3.116	0.920	1.015*	0.984*
HCF life site I	N_H^I	10^5 cycles	Lognormal	0.977	13.58	4.553	2.978	0.471*	1.028*
CCF life site I	N^I	10^4 cycles	Lognormal	0.136	1.377	0.543	0.298	-0.077*	0.752*
LCF life site II	N_L^{II}	10^4 cycles	Lognormal	1.343	5.099	2.700	0.777	0.798*	0.918*
HCF life site II	N_H^{II}	10^6 cycles	Lognormal	0.115	8.119	1.076	1.281	13.12*	3.202*
CCF life site II	N^{II}	10^4 cycles	Lognormal	0.210	2.857	0.995	0.617	0.478*	0.927*

* These values of Kurtosis and Skewness are calculated by transforming the Lognormal distribution to Normal distribution. It is noted that

for variables that are physically non-negative, the corresponding Gaussian priors are truncated at zero. v is specified in the fluid domain and w is specified in the structural domain, the two quantities are physically consistent and derived from the same operating condition.

4.3. Generative meta-modeling

The generative meta-modeling stage develops physics-informed surrogate models capable of representing the conditional distributions under limited simulation data. Each output variable, including output responses ε^{s}_{L}, σ^{s}_{L}, σ^{s}_{H} and the associated lifetimes N^{s}_{L}, N^{s}_{L}, N^{s}_{H} at sites I and II, is approximated using a Transformer-, Diffusion-, or VAE-based generative architecture. The models are trained on the small-batch dataset obtained from the FSI simulations, which capture representative operating ranges for rotational speed, pressures, temperature, stress amplitudes, and strain levels.

(a) Model architecture and hyperparameter configuration

To ensure the transparency and reproducibility of the GenDP framework for distribution-level reliability assessment, this subsection details the network topology and hyperparameter configurations of the adopted generative meta-models. In view of the strongly coupled multi-physics responses of the aeroengine compressor, three conditional generative models (VAE-II, TFM-II, and DFM-II) are adopted to reconstruct the full conditional distributions of responses and lifetimes from limited simulation data. In terms of network topology, all three generative models share a unified three-stage architecture consisting of an input embedding layer, a core generative module, and an output decoding layer. The input embedding layer maps multi-source physical parameters into a latent feature space, the core generative module learns the nonlinear dependencies between inputs and multi-response outputs, and the decoding layer projects latent representations back to the physical response space. GELU activation functions are employed in all hidden layers to facilitate smooth gradient propagation and stable training under complex nonlinear conditions. For model training, all generative models are optimized using the AdamW optimizer. Physical consistency constraints, including stress feasibility and lifetime monotonicity, are imposed as soft penalty terms within a hybrid loss function. This design allows effective exploration of the global stochastic distribution while preserving physical plausibility.

Within the overall optimization framework, network parameters are updated through gradient-based optimization in the inner loop, while key architectural and training hyperparameters are determined by Bayesian optimization in the outer loop. A total of 50 Bayesian optimization trials combined with three-fold cross-validation are conducted to systematically explore the network depth, learning rate scheduling strategy, and noise scheduling parameters. The resulting configurations and corresponding search spaces are summarized in **Table 2**.

Table 2 Generative modeling architecture and hyperparameter configurations

Category	Parameter	VAE-II Search space	TFM-II Search space	DFM-II Search space	VAE-II	TFM-II	DFM-II
Architecture	Hidden size	{128, 256}	{64, 128}	{128, 256}	128	128	128
	Network depth	Enc {2,3} / Dec {2,3}	{2,3,4}	{2,3,4}	Enc 3 / Dec 3	2	2
	Attention heads	—	{4, 8}	—	—	4	—
	FFN size	—	{128, 256, 384}	—	—	128	—
	Latent size	{4, 8, 12}	—	—	12	—	—
	Dropout rate	(0.0, 0.15)	(0.0, 0.15)	(0.0, 0.15)	0.044	0.055	0.028
	Hidden activation	—	—	—	GELU	GELU	GELU
	Output activation	—	—	—	Linear	Linear	Linear
	Time embedding	—	—	Fixed (64)	-	-	64
Training	Learning rate	(5e-4, 3e-3)	(5e-4, 3e-3)	(8e-4, 3e-3)	1.3 e-3	1.3 e-3	1.2 e-3
	Weight decay	(1e-6, 5e-4)	(1e-6, 5e-4)	(1e-6, 3e-4)	1.3 e-4	1.3 e-4	2.0 e-5
	Batch size	{32, 64}	{32, 64}	{32, 64}	64	64	32
	Max epochs	(800, 2000)	(800, 2000)	(800, 2000)	1629	1511	1090
	Early stopping patience	(60, 140)	(60, 140)	(60, 140)	63	63	59
	Diffusion steps	—	—	(60, 150)	—	—	148
	Inference samples	—	—	Fixed	—	—	20
	KL weight	(0.2, 1.5)	—	—	0.68	—	—
	Random seed	Fixed	Fixed	Fixed	42	42	42
	Stress	(1e-4, 5e-2)	(1e-4, 5e-2)	(1e-4, 5e-2)	8e-3	6e-3	1e-2
	Monotonicity	(1e-4, 5e-2)	(1e-4, 5e-2)	(1e-4, 5e-2)	5e-3	4e-3	7e-3
	Fatigue-consistency	(1e-4, 5e-2)	(1e-4, 5e-2)	(1e-4, 5e-2)	3e-3	2e-3	4e-3
HPO	BO trials	—	—	—	50	50	50
Validation	CV folds	—	—	—	3	3	3

Parentheses (;) denote continuous search intervals; braces { } indicate discrete candidate sets; "—" indicates parameters not applicable to the corresponding model; HPO indicates hyperparameter optimization. Parameters marked as fixed are held constant during Bayesian optimization and are not subject to tuning.

(b) Modeling accuracy validation and generalization assessment

To maintain physical interpretability and numerical robustness, the generative models are trained under a hybrid loss that combines data reconstruction, distribution alignment, and explicit physics-informed constraint terms. The physics constraints operate uniformly across all fatigue modes (LCF, HCF, CCF) and both structural failure sites, ensuring global consistency across the hierarchical output space. First, a stress-admissibility constraint is imposed to suppress outputs exceeding material limits; predictions surpassing the allowable range σ_{lim} are penalized, which prevents the model from producing unrealistic stress states regardless of site or fatigue mode. Second, a monotonic lifetime constraint enforces the expected trend that lifetime decreases with increasing rotational speed w and increasing stress amplitude. These physical constraints are applied consistently to all training process, ensuring the generative model preserves the fundamental physical rules across both sites.

As demonstrated by the Taylor diagrams in **Fig. 5**, the DFM-II models achieve high correlation coefficients (0.92-0.99) and low RMSD values across all ten response & lifetime variables. The three-fold cross-validation results in **Fig. 5(a-f)** further show that the proposed method exhibits stable performance across different data partitions, with

consistently high R^2 values and an overall average of approximately 0.982, as well as only minor variations among folds. In comparison with other methods, the proposed approach achieves the highest R^2 while maintaining a low and stable RMSE, indicating robust generalization rather than overfitting to specific training samples. Therefore, the DFM-II model is selected as the representative model for the subsequent assessment tasks. As revealed in **Fig. 6**, the response surfaces further confirm the DFM-II model's ability to reproduce monotonic, nonlinear, and lognormal-type behaviors consistently across multiple sites and fatigue modes. Overall, the data-physics loss-informed generative model provides a coherent and distribution-consistent approximation of multi-site and multi-mode fatigue failure behavior, offering a stable foundation for the subsequent hierarchical reliability assessment.

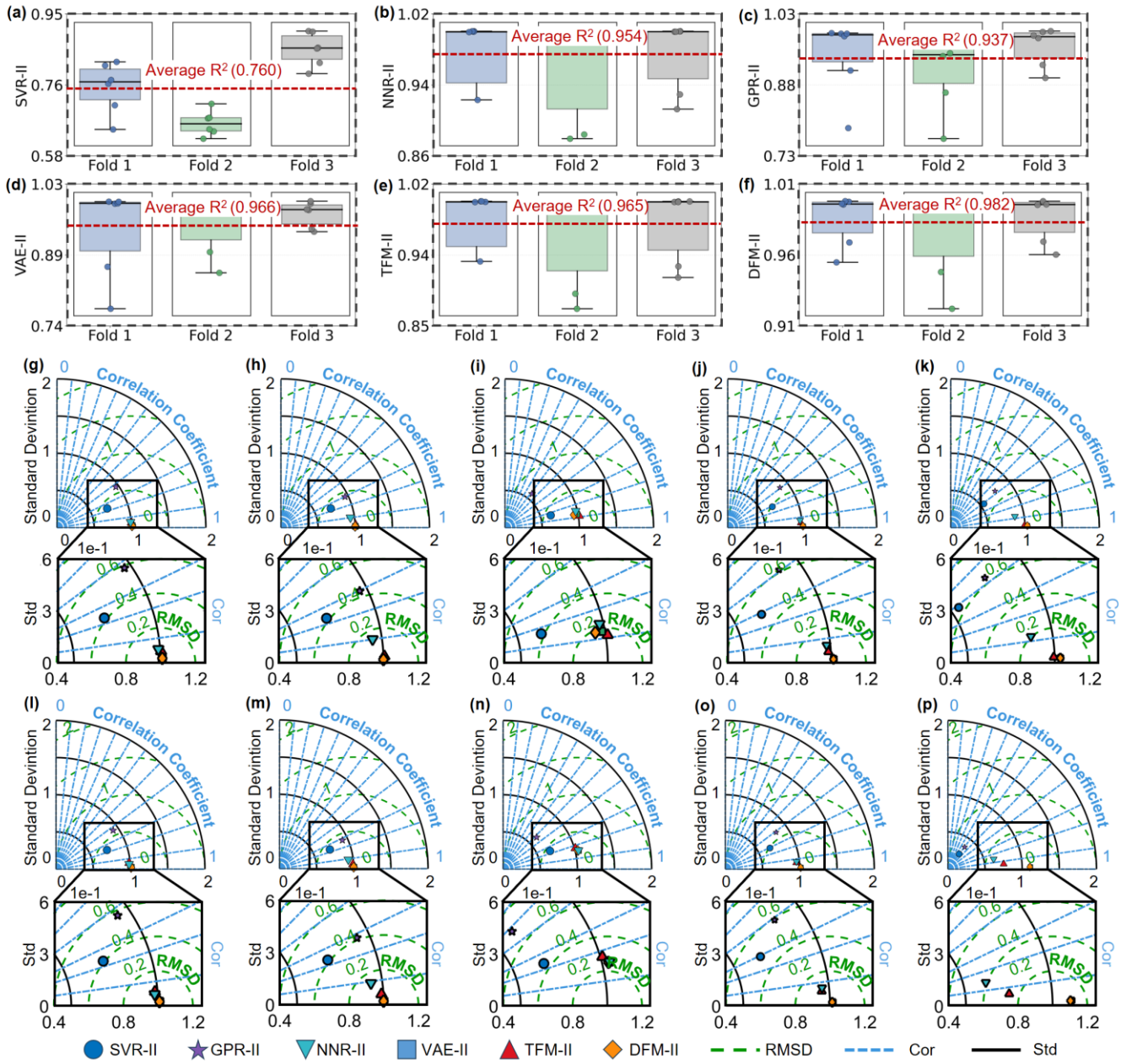

Fig. 5 Modeling accuracy validation of the proposed GenDP fusion (-II indicates using the data-physics thought). Panels (a-f) compare training and validation abilities, respectively. Panels (g-p) show Taylor-diagram-based accuracy validation. (g)$\varepsilon^{\mathrm{I}}{}_{\mathrm{L}}$; (h) $\sigma^{\mathrm{I}}{}_{\mathrm{L}}$; (i) $\sigma^{\mathrm{I}}{}_{\mathrm{H}}$; (j) $N^{\mathrm{I}}{}_{\mathrm{L}}$; (k) $N^{\mathrm{I}}{}_{\mathrm{H}}$; (l) $\varepsilon^{\mathrm{II}}{}_{\mathrm{L}}$; (m) $\sigma^{\mathrm{II}}{}_{\mathrm{L}}$; (n) $\sigma^{\mathrm{II}}{}_{\mathrm{H}}$; (o) $N^{\mathrm{II}}{}_{\mathrm{L}}$; (p) $N^{\mathrm{II}}{}_{\mathrm{H}}$

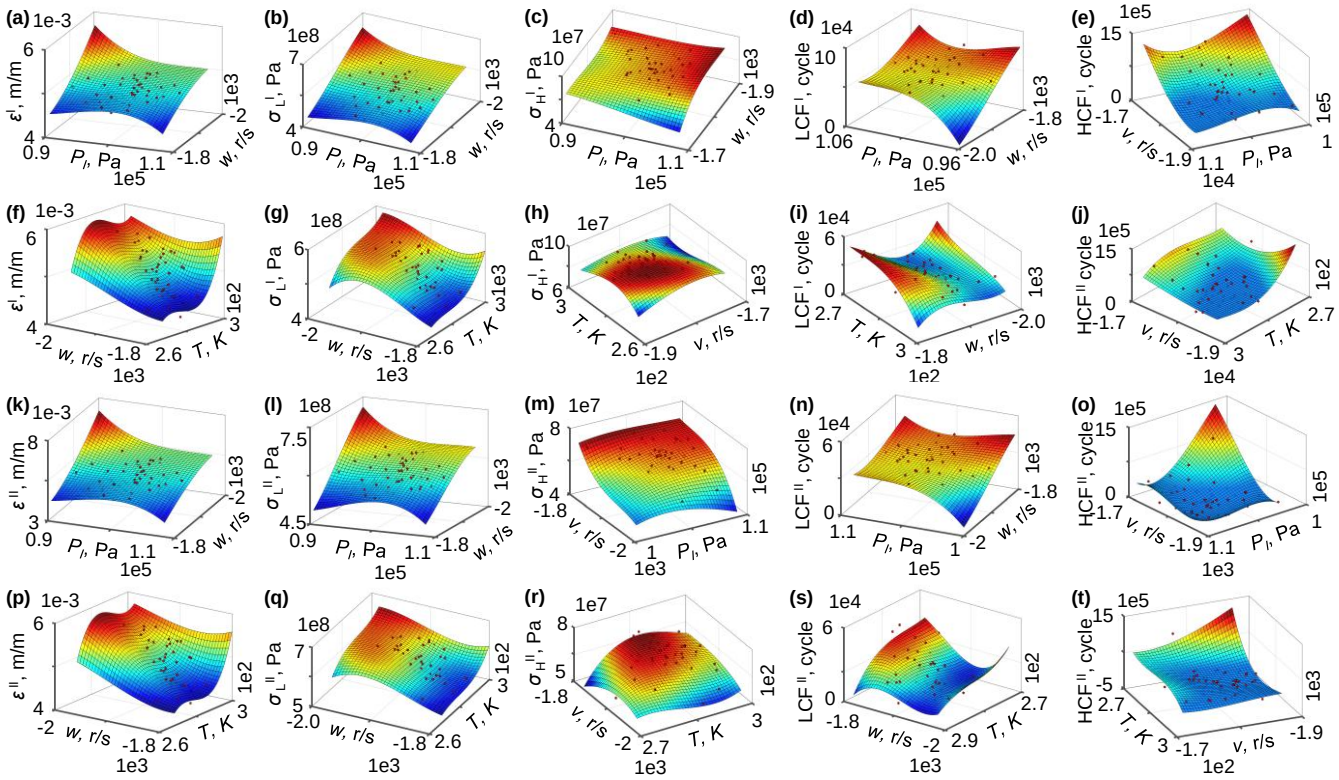

Fig. 6 Response surfaces between output responses and key variables by the DFM-II model. (a) ε^{I}_{L}-P_{I}-w; (b) σ^{I}_{L}-P_{I}-w; (c) σ^{I}_{H}-P_{I}-w; (d) N^{I}_{L}-P_{I}-w; (e) N^{I}_{H}-v-P_{I}; (f) ε^{I}_{L}-w-T; (g) σ^{I}_{L}-w-T; (h) σ^{I}_{H}-T-v; (i) N^{I}_{L}-T-w; (j) N^{I}_{H}-v-T; (k) ε^{II}_{L}-P_{I}-w; (l) σ^{II}_{L}-P_{I}-w; (m) σ^{II}_{H}-v-P_{I}; (n) N^{II}_{L}-P_{I}-w; (o) N^{II}_{H}-v-P_{I}; (p) ε^{II}_{L}-w-T; (q) σ^{II}_{L}-w-T; (r) σ^{II}_{H}-T-v; (s) N^{II}_{L}-T-w; (t) N^{II}_{H}-v-T

5. Hierarchical reliability assessment of the compressor system

This section presents the reliability assessment of the compressor system, emphasizing hierarchical failure dependencies, to demonstrate the effectiveness of the proposed GenDP fusion methodology.

5.1. Response & lifetime prediction

Based on the physics-informed generative models, the probabilistic predictions of site-level responses and fatigue lifetimes are obtained. **Fig. 7** and **Fig. 8** jointly provide an overview of the input uncertainty sources and their propagation through the response and lifetime distributions. **Fig. 7** illustrates the stochastic variations in load-related parameters (P_I, P_O, v, T, w), material properties (ρ, E, α, μ), and fatigue parameters (b, c, σ_f', ε_f'). These uncertainties serve as drivers for the generative sampling process.

Fig. 8 (a-b) present the predicted stress and strain responses at sites I and II. For site I, the LCF stress σ^{I}_{L} spans approximately 4.8×10^{2} to 6.2×10^{2} MPa, with a mean value of 5.28×10^{2} MPa and a standard deviation of 22.68 MPa. The corresponding LCF strain ε^{I}_{L} fluctuates within the range of 4.8×10^{-3} to 6.3×10^{-3} m/m, with a mean value of 5.23×10^{-3} m/m and a standard deviation of 2.45×10^{-4} m/m. The HCF stress σ^{I}_{H} displays a broader spread with values ranging from 70 to 100 MPa, with a mean value of 81.1 MPa and a standard deviation of 5.62 MPa. For site II, the LCF stress σ^{II}_{L} shows a similar distribution, spanning approximately 5.3×10^{2} to 7.0×10^{2} MPa, with a mean value 5.89×10^{2}

MPa and a standard deviation 25.56 MPa. The corresponding LCF strain ε^{II}_{L} varies within 4.5×10^{-3} to 6.3×10^{-3} m/m, exhibiting a mean value of 5.19×10^{-3} m/m and a standard deviation of 2.46×10^{-4} m/m. The HCF stress σ^{II}_{H} spans approximately 50 to 90 MPa, with a mean value of 65.68 MPa and a standard deviation of 5.78 MPa. These probabilistic distribution results confirm that the generative models maintain stable variance characteristics consistent with the small-sample reference behavior.

Fig.8 (c) and (e) show the lifetime predictions in terms of LCF, HCF, and combined-cycle fatigue (CCF). For site I, the CCF life N^{I}_{C} exhibits a right-skewed pattern, consistent with a lognormal distribution commonly observed in fatigue life predictions, with P5 ≈ 9.0×10^{3} cycle, P50 ≈ 1.8×10^{4} cycle, and P95 ≈ 3.5×10^{4} cycle. Moreover, the corresponding CCF life maintains a similar trend, demonstrating the model's ability to reproduce heavy-tail behavior. For site II, the CCF life N^{II}_{C} ranges from approximately 1.0×10^{4} cycle (P5) to 3.9×10^{4} cycle (P95), with a median of about 2.1×10^{4} cycle. **Fig.8 (d)** provides an aggregated view of the normalized statistical levels of lifetimes with respect to different uncertainty groups, including load fluctuations, material variability, and model uncertainty. The values concentrate around 0.45-0.55 for most variables, indicating a balanced distribution of operating conditions and material properties within their respective ranges.

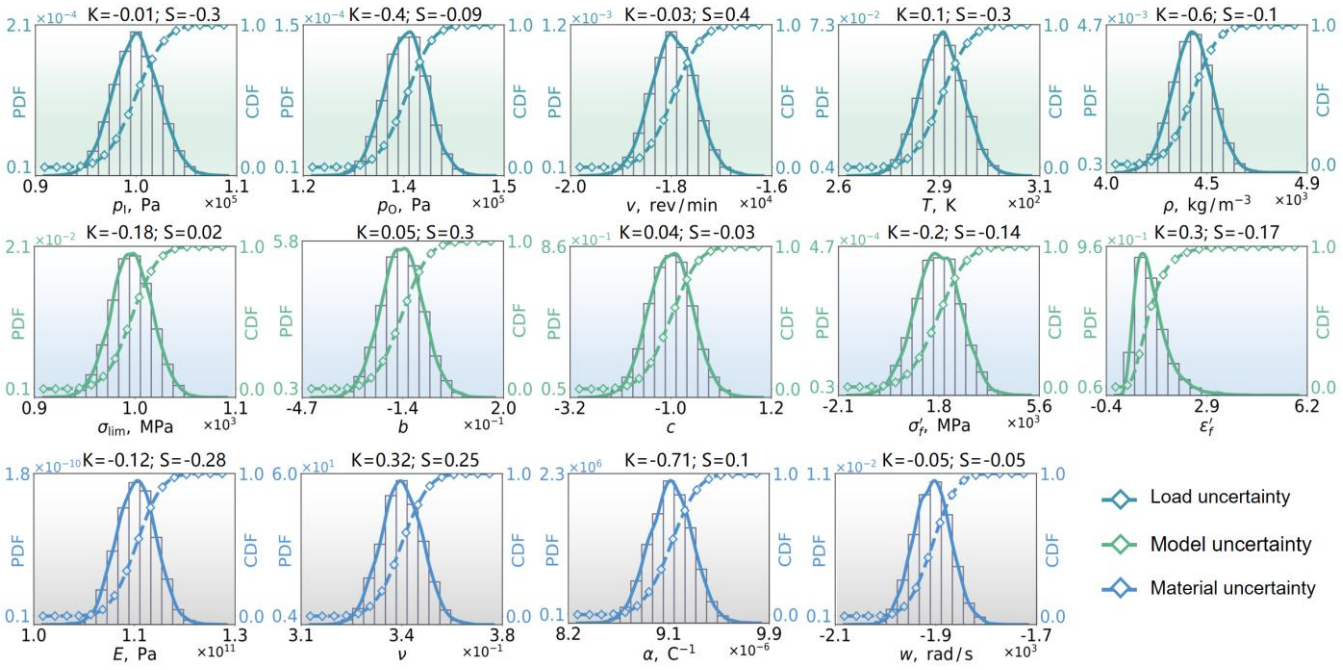

Fig. 7 Probabilistic distributions for Input variables

Fig. 8(f) further illustrates the joint dependency structure between the governing fatigue parameters by means of correlation modeling. Based on the AIC and BIC comparisons, the t copula provides the most suitable fit and is therefore adopted for dependency reconstruction. The smooth and continuous contour patterns indicate that the generated samples capture the coupled variability and nonlinear dependence among fatigue-related variables. This

observation is consistent with the underlying physical correlation structure embedded in the fatigue process. Overall, the generative predictions provide a coherent representation of response variability and lifetime dispersion, serving as suitable inputs for subsequent system-level reliability and sensitivity assessment.

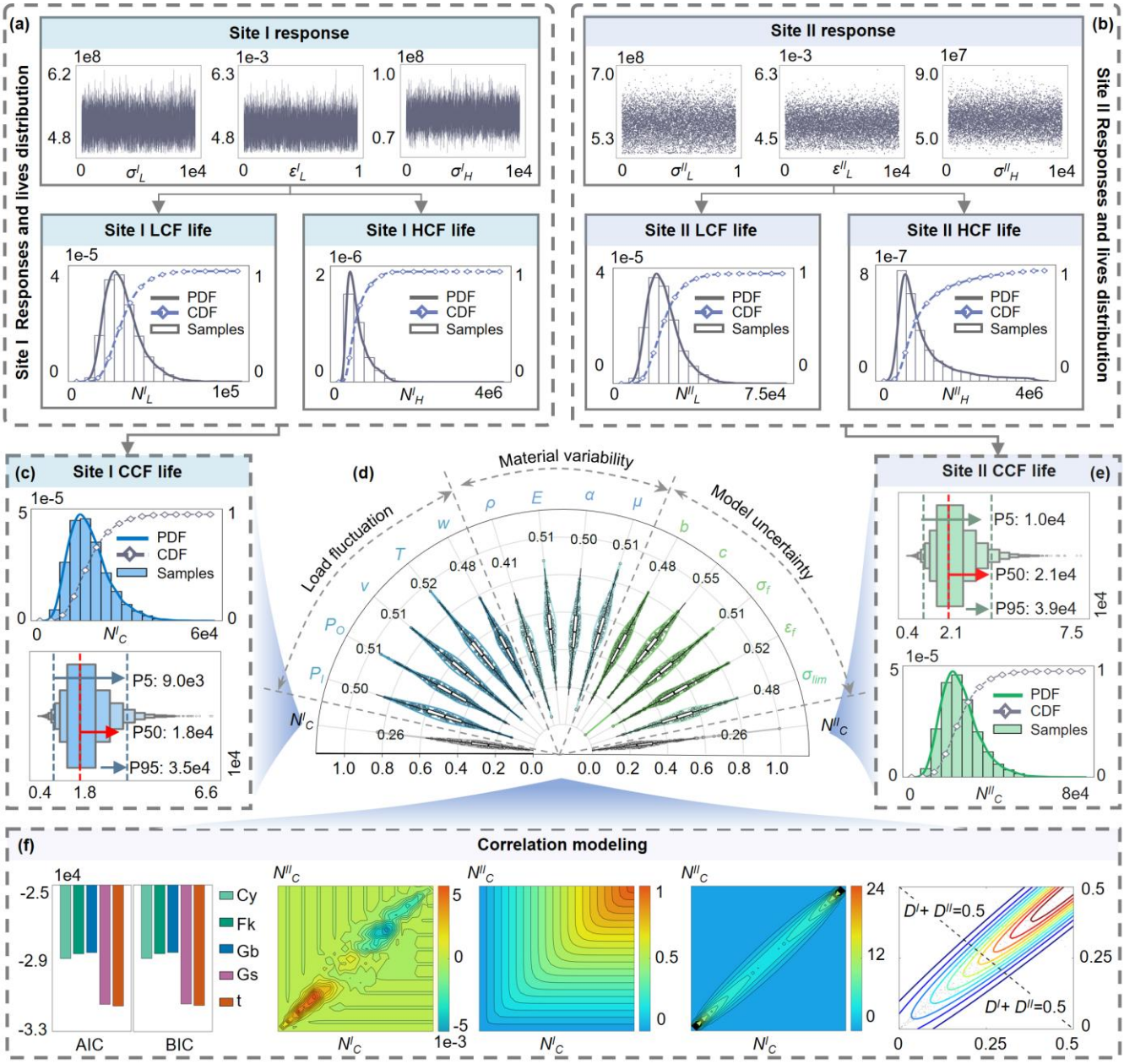

Fig. 8 Probabilistic distributions for responses & lifetimes. (a) Probabilistic distributions of responses at sites I; (b) Probabilistic distributions of responses at sites II; (c) Probabilistic distributions of lifetimes at sites I; (d) Probabilistic distributions of input variables and output responses; (e) Probabilistic distributions of lifetimes at sites II; (f) The correlation between responses

5.2. Correlation quantification

The correlation structure between input variables and hierarchical fatigue responses is examined to clarify the dependence patterns that govern the unit- and system-level behavior. **Fig. 9** summarizes the pairwise associations for low-cycle fatigue (LCF), high-cycle fatigue (HCF), and combined-cycle fatigue (CCF) lifetimes at sites I and II. The graphs in **Figs. 9 (a-f)** visualize the correlation networks for each lifetime response. Variables associated with load fluctuations (P_I, P_O, v, T, w), material properties (ρ, E, α, μ), and fatigue parameters (b, c, σ_f', ε_f') form distinct clusters,

and their connections to output lifetimes provide a clear indication of sensitivity distribution.

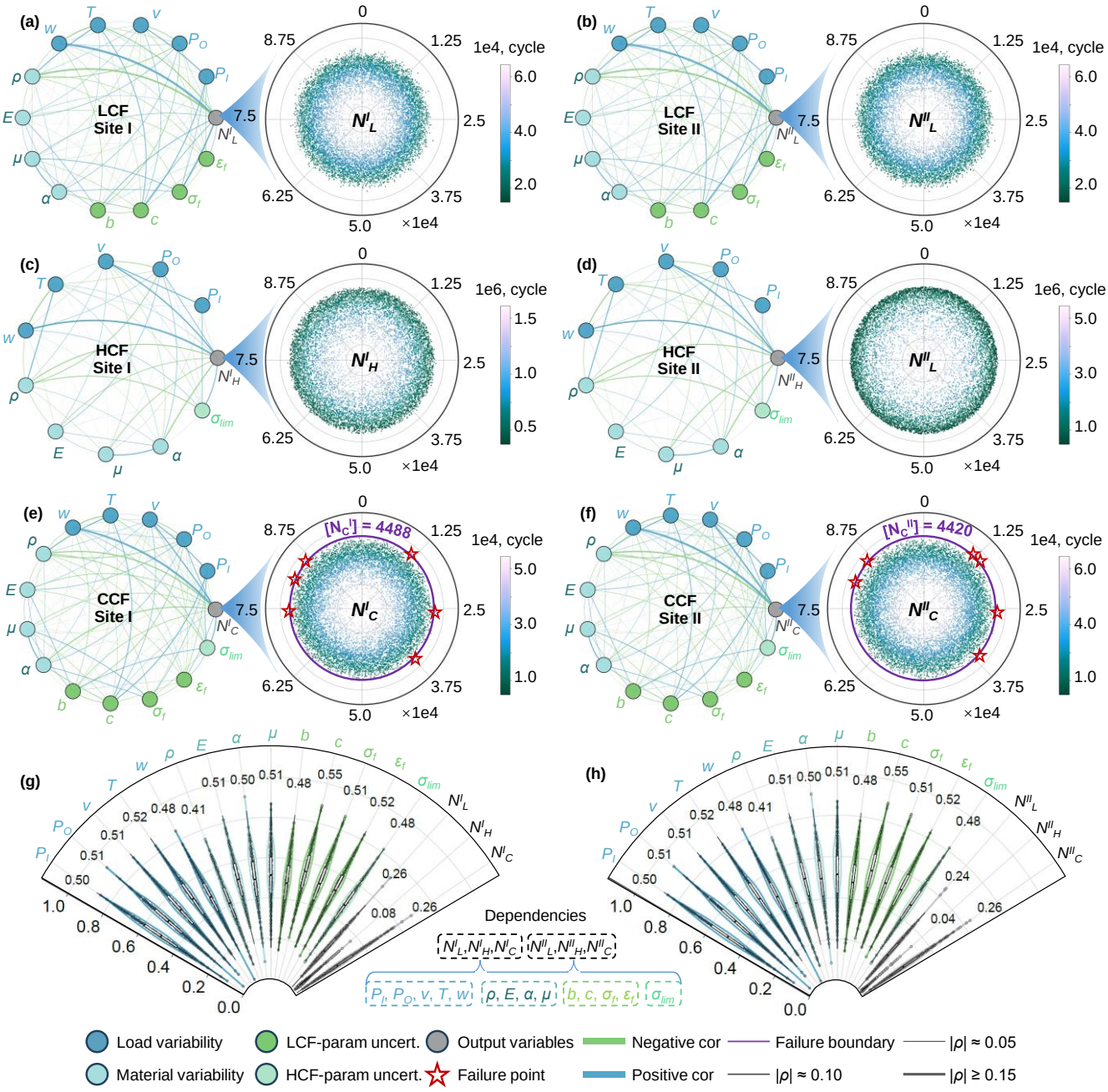

Fig. 9 Correlation quantification for hierarchical variables. Each-site each-mode variables: (a) N^{I}_{L}; (b) N^{II}_{L}; (c) N^{I}_{H}; (d) N^{II}_{H}; (e) N^{I}_{C}; (f) N^{II}_{C}; multi-site multi-mode variables: (g) N^{I}_{L}-N^{I}_{H}- N^{I}_{C}; (h) N^{II}_{L}-N^{II}_{H}- N^{II}_{C}

Fig. 9 provides an integrated view of the relationship structures between uncertainty variables and fatigue lifetimes, together with the corresponding lifetime dispersion characteristics. Subplots (a), (c), and (e) present the LCF, HCF, and CCF lives at site I, while subplots (b), (d), and (f) show the corresponding results at site II. In each case, the left panels depict relationship networks, where blue and green edges indicate positive and negative relationships, respectively, and edge weight reflects the relative strength of the relationship. Load-related parameters, including inlet/outlet pressures and rotational speed, exhibit relatively strong relationships with the lifetime responses at both sites, whereas parameters such as temperature show moderate influence. The right panels display circular scatter plots

of the predicted lifetimes, illustrating the dispersion behavior under combined uncertainty effects. Compared with LCF, the HCF lifetimes exhibit noticeably wider spreads, reaching the order of 10^6 cycles, while the LCF lifetimes remain more concentrated around the order of 10^4cycles. For the CCF cases shown in subplots (e) and (f), failure points are highlighted by red pentagrams, and the allowable CCF lives specified as $[N^{\mathrm{I}}_C]$ =4488 cycles for site I and $[N^{\mathrm{II}}_C]$ = 4420 cycles for site II, indicating consistent failure thresholds across the two structural locations. The bottom panels (g) and (h) summarize the overall distributions of the input uncertainty variables and output lifetime responses, providing an aggregated view of their statistical spread across different uncertainty groups.

5.3. Hierarchical reliability & sensitivity evaluation

The hierarchical reliability characteristics of the compressor are evaluated using the generative distribution outputs and their propagation through the fatigue models. **Fig. 10(a-b)** first presents the cumulative distribution functions of the predicted damage metrics for LCF and HCF at sites I and II. For site I (**Fig. 10(a)**), the LCF damage $D^{\mathrm{I}}_{\mathrm{L}}$ gradually increases with cycle counts from 1×10^3 to 6×10^3, showing a continuous rightward shift of the CDF curves. The same trend is observed for HCF damage $D^{\mathrm{I}}_{\mathrm{H}}$, although the increments are more moderate, reflecting the higher-cycle nature of the HCF process. Site II responses (**Fig. 10(b)**) exhibit similar monotonic behavior, with damage levels generally lower than those at site I due to reduced local stress concentration. These results indicate that the generative models are able to reproduce physically consistent damage accumulation across different cycle ranges.

Fig. 10(c-d) compares the reliability responses of LCF, HCF, and CCF lives for sites I and II, together with the combined system-level behavior. For both sites, the CCF reliability curve lies below the corresponding LCF- and HCF-dominated responses, indicating that the combined-cycle fatigue reliability is governed by the concurrent action of low- and high-cycle damage mechanisms and is therefore more conservative. The influence of inter-site dependence on the combined reliability response is further reflected by the comparison between independent and dependent assumptions: the independent case yields a higher combined reliability, whereas accounting for inter-site correlation leads to a further downward shift of the reliability curve and thus a more conservative estimate. Overall, the results highlight the integrated effects of multi-site interaction and multi-mode fatigue coupling on the system-level fatigue reliability. **Fig. 10(d)** is the overall system reliability, from which a design-relevant reliability level of 0.9987 corresponds to a fatigue life of approximately 3944 cycles.

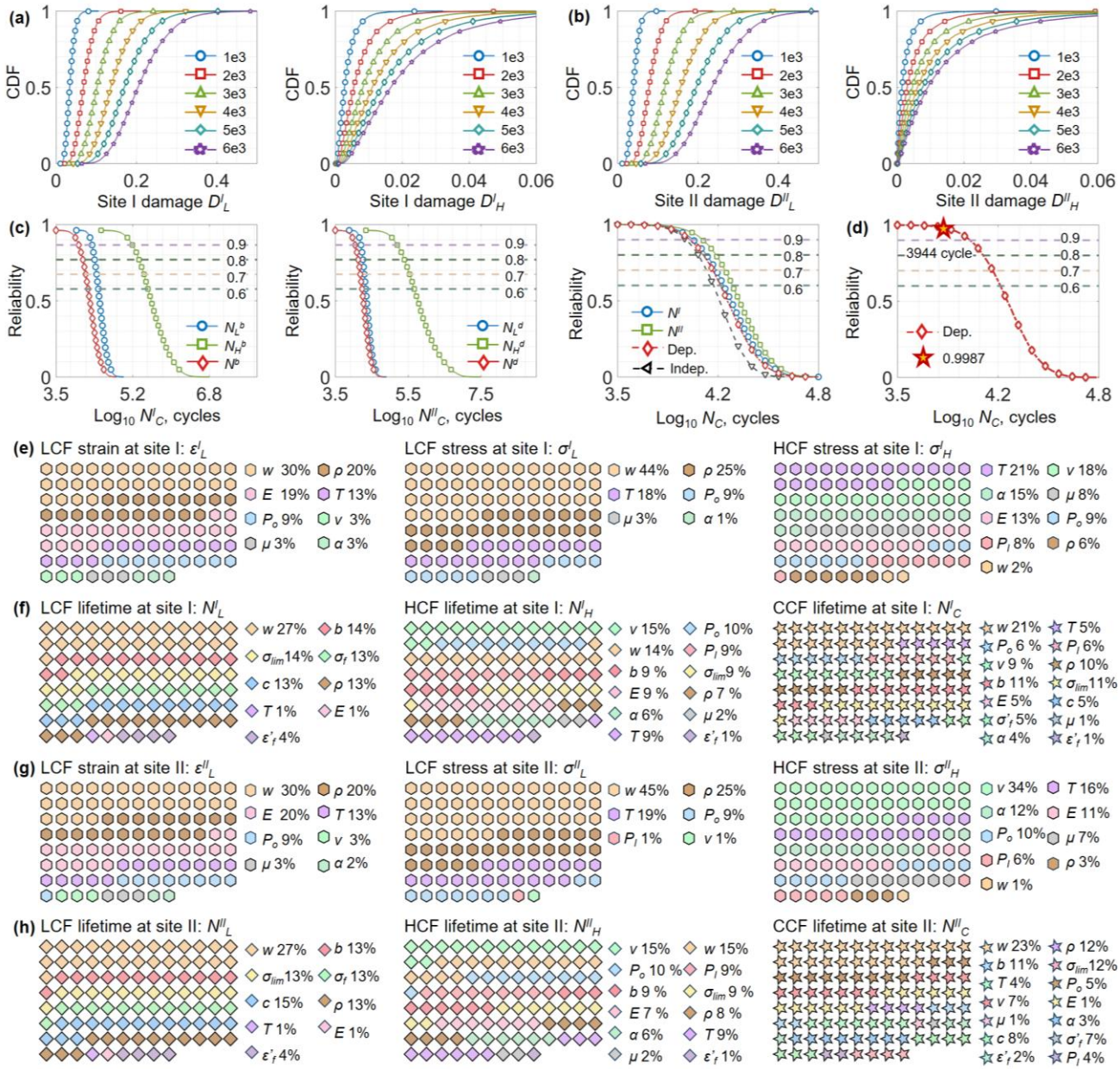

Fig. 10 Reliability and sensitivity for hierarchical structural system. (a) fatigue damage at site I; (b) fatigue damage at site II; (c) reliability under each-site and multi-site; (d) reliability with failure correlation; (e) response sensitivity at site I; (f) response sensitivity at site II; (g) lifetime sensitivity at site I; (h) lifetime sensitivity at site II

Sensitivity analyses for strain, stress, and all lifetime responses are shown in **Fig. 10(e-h)**. For site I strain (**Fig. 10(e)**), rotational speed w accounts for approximately 30%, followed by outlet pressure P_O at 20%, temperature T at 19%, and inlet pressure P_I at 9%, while Material variables E and ρ contribute around 7-3%. Stress sensitivities at site I indicate dominant contributions from w (44%), T (18%), and P_O (25%). HCF stress sensitivities emphasize fatigue strength σ_f' (21%) and ductility parameter ε_f' (18%), consistent with high-cycle response characteristics. Lifetime sensitivities (**Figs. 10(f-h)**) present broader distributions, LCF lifetime N^{I}_{L} is mainly driven by w (27%), σ_f' (14%), and c (13%), followed by T (12%). HCF lifetimes emphasize σ_f' (15%) and ε_f' (10%) along with moderate contributions from load variables (9-7%). CCF sensitivity patterns show mixed influence, with w reaching 21-23% at both sites, and fatigue parameters (σ_f') accounting for 10-17%. Overall, the hierarchical reliability and sensitivity outcomes highlight

the roles of load fluctuation, material variability, and fatigue parameter scatter across structural sites. The dependent reliability model yields more realistic reliability decay trends, and the sensitivity distributions provide interpretable guidance for targeted uncertainty reduction and design refinement.

5.4. Comparisons & discussions

The performance of the developed surrogates is evaluated by comparing their computational efficiency and predictive accuracy against several reference models. For clarity in the comparison, the variants enhanced through the data-physics fusion strategy are denoted by "-II," and their corresponding data-driven versions by "-I." The generative surrogates tested in this study, alongside the traditional regression models, including SVR-I, GPR-I, and NNR-I, provide a representative set of approaches for examining large-scale fatigue behavior. **Fig. 11** reports the comparative results for site I, site II, and the multisite system across different sample sizes. It is noted that the sample sizes ranging from 100 to 10,000 refer to the number of Monte Carlo (MC) samples used to construct the reference reliability estimates, rather than the training data size of surrogate models. The modeling performance of the proposed approach has already been demonstrated in **Fig. 5**, and the MC-based analysis here is used solely to assess the reliability estimation behavior under increasingly accurate reference solutions.

Fig. 11(a-d) reports the computational efficiency of each surrogate relative to the direct Monte Carlo simulation benchmark. For site I (**Fig. 11(a)**), the DFM-II model demonstrates consistently high acceleration factors, achieving efficiency gains in the range of 138-168× depending on the sampling size. In contrast, traditional regression surrogates such as SVR-I and GPR-I exhibit more modest improvements, typically around 80-120×. Similar observations are found at site II (**Fig. 11(b)**), where the efficiency of DFM-II surpasses 150× at the largest sampling level, while baseline models remain below 130×. For the multisite reliability assessment (**Fig. 11(c)**), the advantage of the fusion-based generative surrogate becomes more evident, benefiting from its ability to generate coherent multi-output samples at negligible cost. **Fig. 11(d)** shows the absolute execution time, where DFM-II maintains substantially shorter runtime compared to other models across all sampling levels, reaffirming its computing scalability.

Fig. 11(e-h) presents the reliability accuracy compared with Monte Carlo reference results. For site I (**Fig. 11(e)**), the DFM-II model consistently reaches accuracy levels above 97%, even at relatively small sample sizes. SVR-I and GPR-I remain within a similar but slightly lower band (92-96%), whereas VAE-I displays larger fluctuations. The accuracy trends at Site II (**Fig. 11(f)**) show a similar structure, with DFM-II maintaining 96-98% accuracy and conventional surrogates showing broader variability. The system reliability results (**Fig. 11(g)**) confirm that DFM-II preserves accuracy above 97% across all sampling scales, which is essential for dependent reliability evaluation. Finally, **Fig. 11(h)** compares the actual reliability values estimated by different methods. The DFM-II predictions match closely

with the Monte Carlo baseline, whereas other models yield slightly biased estimates in high-sensitivity regions. In **Fig. 11(e-h)** prediction performance is evaluated using a relative accuracy metric, defined as $Acc_{rel}=1-|R_{SM}-R_{MC}|/R_{MC}$, where R_{SM} denotes the reliability estimate obtained from the surrogate model and R_{MC} represents the MC-based result. This metric reflects the deviation of surrogate predictions relative to the MC reference. **Fig. 11(i-k)** reports the absolute error of the reliability estimates, defined as $\varepsilon_{abs}=|R_{SM}-R_{MC}|$, which provides a direct measure of the discrepancy on a common probability scale between surrogate-based and MC-based reliability estimates. The results show that reliability estimation accuracy improves with increasing Monte Carlo sample sizes, with the proposed method achieving the highest overall accuracy. The inset bar charts further demonstrate that the "-II" models yield substantial accuracy improvements over their "-I" counterparts across all model families. **Fig. 11(l)** summarizes the efficiency improvement factor under the multi-site setting.

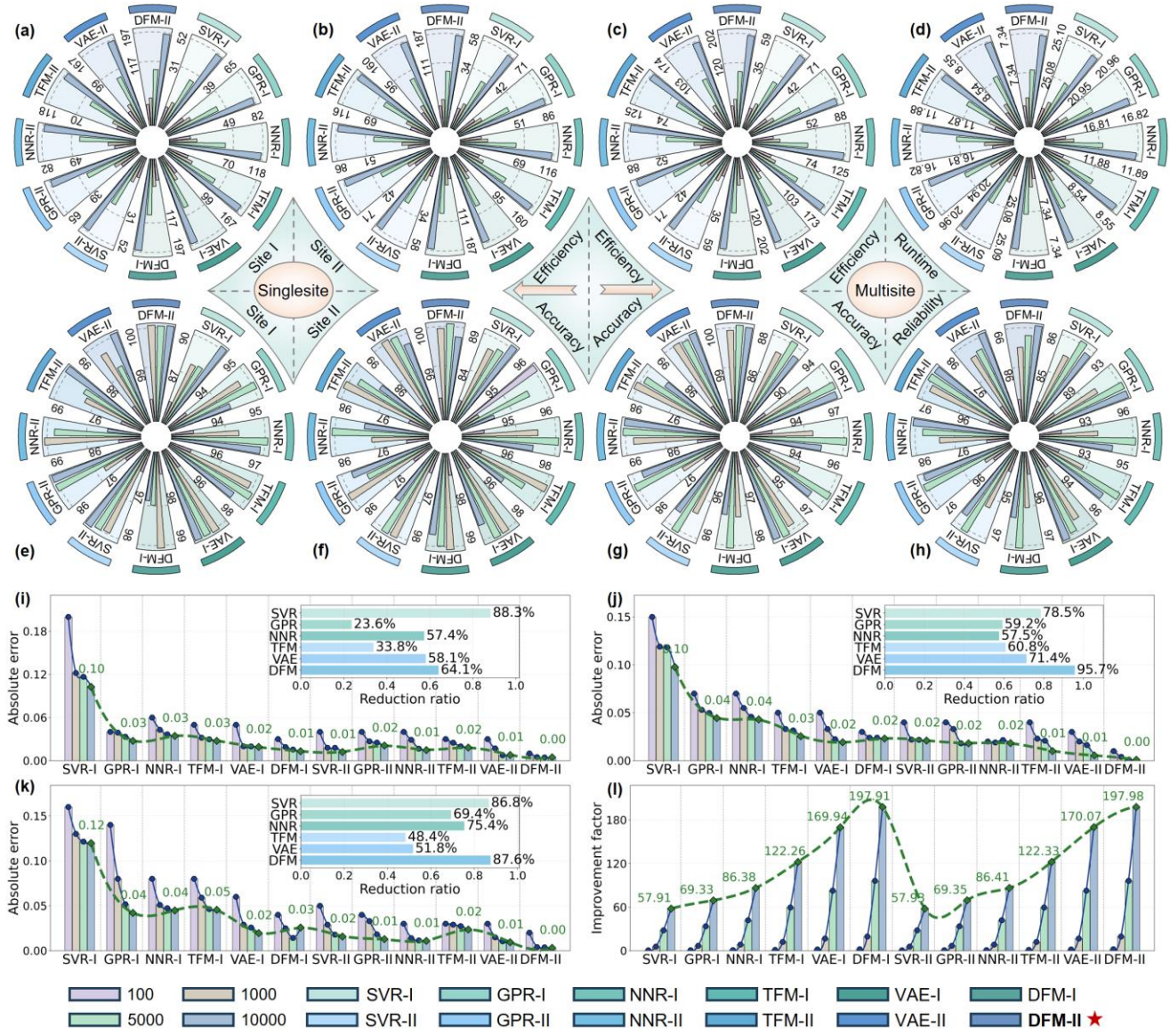

Fig. 11 Method comparisons under different simulation accuracy & efficiency. (a) simulation efficiency under site I; (b) simulation efficiency under site II; (c) simulation efficiency under multi-site; (d) simulation runtime under multi-site; (e) simulation accuracy under site I; (f) simulation accuracy under site II; (g) simulation accuracy under multi-site; (h) system reliability under multi-site; (i) absolute error under site I; (j) absolute error under site II; (k) absolute error under multi-site; (l) efficiency improvement factor under multi-site

Overall, these comparisons demonstrate three consistent observations. Firstly, the proposed generative data-physics fusion surrogate achieves substantial computational savings without compromising precision, allowing large-scale reliability estimation under strict computational budgets. Secondly, the accuracy advantage becomes more pronounced for hierarchical and multisite reliability problems, owing to the generative model's ability to maintain joint distribution features across sites. Thirdly, the stability across sample sizes indicates reliable extrapolation behavior under limited data, which is critical for real engineering systems where obtaining large simulation datasets is often infeasible. These findings verify that the proposed approach provides a balanced and effective tool for hierarchical reliability assessment while delivering both high computing efficiency and high predictive accuracy.

6. Conclusions

This study establishes a generative data-physics (GenDP) fusion framework for hierarchical reliability assessment of complex dependent systems. The proposed GenDP fusion framework integrates physics-based hierarchical decomposition with physics-informed generative modeling, forming a coherent pathway that transforms small-batch simulation data into distribution-level representations suitable for large-scale hierarchical reliability evaluation. A representative aeroengine compressor system is employed to validate the proposed framework. The main findings of this study are summarized as follows:

(1) The proposed GenDP fusion framework organizes multi-site and multi-mode failure processes through a hierarchical-generative structure, where the hierarchical layer provides physically interpretable decomposition and the generative layer learns full conditional distributions of responses and lifetimes, thereby preserving both physical interpretability and distributional representation.

(2) By embedding stress limits, monotonicity requirements, and fatigue-law consistency into Transformer-, Diffusion-, and VAE-based generative models, the proposed approach overcomes the pointwise limitations of conventional surrogates. The resulting data-physics-aligned distributions support accurate tail-sensitive reliability estimation without relying on high-volume simulation or restrictive assumptions.

(3) A physics-constrained sampling strategy directs data generation toward physically admissible and near-failure regions, and a Copula dependency formulation reconstructs cross-site and cross-mode correlations. This enables a consistent hierarchical-to-system reliability propagation process, ensuring that component-level uncertainties translate realistically into system-level behaviors.

(4) The aeroengine compressor case study demonstrates the effectiveness of the proposed framework. Quantitative comparisons against direct Monte Carlo simulations demonstrate a computational speed-up of 138×-168× while

maintaining reliability calculation accuracy above 97%. Furthermore, the framework exhibits robust performance, with accuracy fluctuations restricted to within a 2% margin (96%-98%) across varying sample sizes, confirming its stability and potential for broader engineering applications.

Future research will explore extensions toward time-variant reliability, multi-physics ageing processes, hybrid generative physics operators for digital-twin updating, and integration with real-time monitoring data, aiming to further enhance data efficiency and system-level predictive reliability in complex engineering environments.

Acknowledgement

This paper is co-supported by Beijing Natural Science Foundation (Grant no. 24JL002), National Natural Science Foundation of China (Grant no. 52105136), Beijing Outstanding Young Scientist Program, and New Cornerstone Science Foundation through the XPLORER PRIZE. The authors would like to thank them.

The authors would also like to note that Matthias Faes is an Associate Editor of this journal. In accordance with editorial policy, Matthias Faes was fully blinded to the entire peer-review process.

Declaration of competing interests

The authors declare that they have no known competing financial interests or personal relationships that could have appeared to influence the work reported in this paper.

CRediT authorship contribution statement

Lu-Kai Song: Writing-original draft, Conceptualization, Methodology, Investigation, Visualization.

Matthias G.R. Faes: Writing-review & editing, Conceptualization, Validation, Investigation.

Fei Tao: Writing-review & editing, Funding acquisition, Validation, Project administration, Resources.

References

[1] Mozafari S, Veers PS, Rinker J, Dykes K. Sensitivity of fatigue reliability in wind turbines: effects of design turbulence and the Wöhler exponent, Wind Energy Science, 2024, 9(4): 799-820.

[2] Liao D, Zhu SP, Correia JAFO, De Jesus AMP, Veljkovic M, Berto F. Fatigue reliability of wind turbines: historical perspectives, recent developments and future prospects, Renewable Energy, 2022, 200: 724-742.

[3] Afshari SS, Zhao C, Zhuang X, Liang X. Deep learning-based methods in structural reliability analysis: a review, Measurement Science and Technology, 2023, 34(7): 072001.

[4] Quinci G, Paolacci F, Fragiadakis M, Bursi OS. A machine learning framework for seismic risk assessment of industrial equipment, Reliability Engineering & System Safety, 2025, 254: 110606.

[5] Aryai V, Abbassi R, Abdussamie N, Salehi F, Garaniya V, Asadnia M, Baksh AA, Penesis I, Karampour H, Draper S, Magee A, Keng AK, Shearer C, Sivandran S, LimKY, Cook D, Underwood M, Martini A, Heasman K, Abrahams J, Wang CM. Reliability of multi-purpose offshore-facilities: present status and future direction in Australia, Process Safety and Environmental Protection, 2021, 148: 437-461.

[6] Niu XP, Wang RZ, Liao D, Zhu SP, Zhang XC, Keshtegar B. Probabilistic modeling of uncertainties in fatigue reliability analysis of turbine bladed disks, International Journal of Fatigue, 2021, 142: 105912.

[7] Mardfekri M, Gardoni P. Multi-hazard reliability assessment of offshore wind turbines, Wind Energy, 2015, 18(8): 1433-1450.

[8] Teng D, Feng YW, Chen JY, Lu C. Structural dynamic reliability analysis: review and prospects, International Journal of Structural Integrity, 2022, 13(5): 753-783.

[9] Zhang B, Wang W, Wang Y, Li Y, Li CQ. A critical review on methods for time-dependent structural reliability, Sustainable and Resilient Infrastructure, 2024, 9(2): 91-106.

[10] Ayoob K, Elahi H, Zafar T, Hamza A, Wang Z. Surrogate modeling for time-dependent reliability analysis of robotic manipulator trajectories, PLOS One, 2025, 20(9): e0331502.

[11] Zhao Z, Lu ZH, Zhao YG. Time-variant reliability analysis using moment-based equivalent gaussian process and importance sampling, Structural and Multidisciplinary Optimization, 2022, 65(2): 73.

[12] Tempelis A, Jespersen KM, Mishnaevsky LJr. Fatigue damage mechanics approach to predict the end of incubation and breakthrough of leading edge protection coatings for wind turbine blades, International Journal of Fatigue, 2025, 190: 108617.

[13] Slot RM, Sørensen JD, Sudret B, Svenningsen L, Thøgersen ML. Surrogate model uncertainty in wind turbine reliability assessment, Renewable Energy, 2020, 151: 1150-1162.

[14] Li M, Wang Z. Deep learning for high-dimensional reliability analysis, Mechanical Systems and Signal Processing, 2020, 139: 106399.

[15] Drucker H, Burges C J, Kaufman L, Smola A, Vapnik V. Support vector regression machines, Advances in Neural Information Processing Systems, 1996, 9.

[16] Lyu H, Li Z, Qiao X, Lu B, Xie H, Pecht M. Reliability analysis for multi-component system considering failure propagation and dependent competing failure process, Reliability Engineering & System Safety, 2025, 259: 110930.

[17] Kim G, Kwag S, Eem S, Hahm DG, Park JH. Probabilistic safety assessment of off-site power system under typhoon considering failure correlation between transmission towers, Reliability Engineering & System Safety, 2025, 254: 110637.

[18] Li XQ, Song LK, Bai GC. Failure correlation evaluation for complex structural systems with cascaded synchronous regression, Engineering Failure Analysis, 2022, 141: 106687.

[19] Song LK, Bai GC, Li XQ, Wen J. A unified fatigue reliability-based design optimization framework for aircraft turbine disk, International Journal of Fatigue, 2021, 152: 106422.

[20] Yang LC, Zhang XH, Zhu F, Wang Z, Zhang XG. Semi-supervised cross-domain fault diagnosis via contrastive pre-training and annotation-efficient alignment strategy, Journal of Industrial Information Integration, 2026, 50: 101076.

[21] Song LK, Tao F, Choy Y, Yang LC, Wei YF. Cascade sampling-driven block mapping for coupled reliability evaluation of turbine cooling systems, Mechanical Systems and Signal Processing, 2025, 236: 113008.

[22] Shi LJ, Zhou K, Wang, ZQ. Convolutional dimension-reduction with knowledge reasoning for reliability approximations of structures under high-dimensional spatial uncertainties. Journal of Mechanical Design, 2024, 146(7): 071701.

[23] Zhou K, Enos R, Zhang DY, Tang J. Uncertainty analysis of curing-induced dimensional variability of composite structures utilizing physics-guided Gaussian process meta-modeling. Composite Structures, 2022, 280: 114816.

[24] Behrendt M, Faes MGR, Valdebenito MA, Beer M. Estimation of an imprecise power spectral density function with optimised bounds from scarce data for epistemic uncertainty quantification, Mechanical Systems and Signal Processing, 2023, 189: 110072.

[25] Yang LC. An evidence-based likelihood approach for the reliability of a complex system with overlapped failure data, Computers & Industrial Engineering, 2025, 201: 110893.

[26] Li XQ, Song LK, Bai GC, Li DG. Physics-informed distributed modeling for CCF reliability evaluation of aeroengine rotor systems, International Journal of Fatigue, 2023, 167: 107342.

[27] Li XQ, Song LK, Choy YS, Bai GC. Fatigue reliability analysis of aeroengine blade-disc systems using physics-informed ensemble learning, Philosophical Transactions of the Royal Society A, 2023, 381(2260): 20220384.

[28] Jafari-Asl J, Dong Y, Guo H. Enhancing Structural Reliability through AI-Driven Control Variates and Subset Simulation, ASCE-ASME Journal of Risk and Uncertainty in Engineering Systems, Part A: Civil Engineering, 2025, 11(4): 04025056.

[29] Joseph J, Swalih CK A. Implementation of machine learning in structural reliability analysis. Journal of Civil Engineering and Materials Application, 2023, 7(3): 131-137.

[30] Li XQ, Song LK, Bai GC. Deep learning regression-based stratified probabilistic combined cycle fatigue damage evaluation for turbine bladed disks, International Journal of Fatigue, 2022, 159: 106812.

[31] Zhan H, Xiao NC. Expected lifetime prediction for time- and space-dependent structural systems based on active learning surrogate model, Computer Methods in Applied Mechanics and Engineering, 2024, 429: 117150.

[32] Li XQ, Song LK, Choy YS, Bai GC. Multivariate ensembles-based hierarchical linkage strategy for system reliability evaluation of aeroengine cooling blades, Aerospace Science and Technology, 2023, 138: 108325.

[33] Song LK, Tao F, Li XQ, Yang LC, Wei YP, Beer M. Physics-embedding multi-response regressor for time-variant system reliability assessment, Reliability Engineering & System Safety, 2025, 263: 111262.

[34] Song LK, Li XQ, Zhu SP, Choy YS. Cascade ensemble learning for multi-level reliability evaluation, Aerospace Science and Technology, 2024, 148: 109101.

[35] Acevedo CH, Zhang XY, Valdebenito MA, Faes MGR. Reliability analysis combining method of moments with control variates, Probabilistic Engineering Mechanics, 2025, 81: 103771.

[36] Manque NA, Liedmann J, Barthold FJ, Valdebenito MA, Faes MGR. Interval isogeometric analysis for coping with geometric uncertainty, Computer Methods in Applied Mechanics and Engineering, 2025, 437: 117773.

[37] Lahmar S, Maalmi M, Idchabani R. Investigating adaptive sampling strategies for optimal building energy performance using artificial neural networks and kriging surrogate models, Journal of Building Engineering, 2024, 82: 108341.

[38] Wenzel S, Slomski-Vetter E, Melz T. Optimizing system reliability in additive manufacturing using physics-informed machine learning, Machines, 2022, 10(7): 525.

[39] Yu F, Wu X, Yu S. Kriging-based time-variant reliability analysis incorporating error distance function and first crossing time point,

Applied Sciences, 2025, 15(10): 5257.

[40] Li YF, Feng J, Qian HM, Huang T, Huang HZ. Outcrossing rate-based time-variant reliability analysis method under multiple failure modes, Quality and Reliability Engineering International, 2025, 41(8): 3396-3404.

[41] Shanks BL, Sullivan HW, Shazed AR, Hoepfner MP. Accelerated bayesian inference for molecular simulations using local gaussian process surrogate models, Journal of Chemical Theory and Computation, 2024, 20(9): 3798-3808.

[42] Yu S, Wu X, Zhao D, Li Y. A two-level surrogate framework for demand-objective time-variant reliability-based design optimization, Reliability Engineering & System Safety, 2024, 244: 109924.

[43] Chen JY, Feng YW, Teng D, Pan WH, Liu JQ. Dimensionality reduction-based extremum surrogate modeling strategy for transient reliability analysis of complex structures, Engineering Failure Analysis, 2021, 130: 105745.

[44] Yu S, Wang Z, Li Y. Time and space-variant system reliability analysis through adaptive kriging and weighted sampling, Mechanical Systems and Signal Processing, 2022, 166: 108443.

[45] Singh PK, Farrell-Maupin KA, Faghihi D. A framework for strategic discovery of credible neural network surrogate models under uncertainty, Computer Methods in Applied Mechanics and Engineering, 2024, 427: 117061.

[46] Song LK, Bai GC, Li XQ. A novel metamodeling approach for probabilistic LCF estimation of turbine disk, Engineering Failure Analysis, 2021, 120: 105074.

[47] Song LK, Tao F, Peng G Z. Mixed loss-guided modular regression for dependent system reliability, Reliability Engineering & System Safety, 2026, 267: 111898.

[48] Chen X, Ma M, Zhao Z, Zhai Z, Mao Z. Physics-informed deep neural network for bearing prognosis with multisensory signals, Journal of Dynamics, Monitoring and Diagnostics, 2022: 200-207.

[49] Kulkarni NN, Sabato A. Full-field expansion and damage detection from sparse measurements using physics-informed variational autoencoders, Structural Health Monitoring, 2026, 25(1): 607-629.

[50] Wang H, Li B, Lei L, Xuan F. Multi-physics information-integrated neural network for fatigue life prediction of additively manufactured Hastelloy X superalloy, Virtual and Physical Prototyping, 2024, 19(1): e2368652.

[51] Chen Y, Li Y, Li G, Liu H, Lu Z. Data augmentation of gear fatigue test using generative adversarial networks, Journal of Mechanical Science and Technology, 2025, 39(9): 5051-5063.

[52] Nouri A, Zamani A, Toufigh V. A physics-informed data-driven framework for structural health monitoring of thermal fatigue in concrete composites, Structural Health Monitoring, 2025: 14759217251375838.

[53] Lu YW, Wang Y, Liu X, Zhang C, Hsu CY. Physics-informed machine learning for failure mode proportion prediction in composite adhesive joints, Journal of Manufacturing Science and Engineering, 2025, 147(8): 081007.

[54] Wang J, Yao L, He Z, Lomov SV, Carvelli V, Tat KE, Sapozhnikov SB. Physics-informed machine learning model for mode I fatigue delamination growth in composite laminates under different load ratios, Composites Part B: Engineering, 2025, 113074: 113074.

[55] Shi L, Wang Z. High-dimensional reliability estimation of engineered structures using deep networks and adaptive hierarchical learning, Engineering Structures, 2025, 340: 120657.

[56] Chen J, Liu Y. Probabilistic physics-guided machine learning for fatigue data analysis, Expert Systems with Applications, 2021, 168: 114316.

[57] Chen D, Hong W, Zhou X. Transformer network for remaining useful life prediction of lithium-ion batteries, IEEE Access, 2022, 10: 19621-19628.

[58] Zhang Z, Song W, Li Q. Dual-aspect self-attention based on transformer for remaining useful life prediction, IEEE Transactions on Instrumentation and Measurement, 2022, 71: 1-11.

[59] Lin Y, Guo Q, Cai W, Zhang X, Yang L. Remaining useful life prediction of SiC MOSFETs based on SVMD-SSA-transformer model, Electronics, 2025, 14(21): 4284.

[60] Feng F, Zhu T, Yang B, Zhang Z, Zhou S, Xiao S. Probabilistic fatigue life prediction in additive manufacturing materials with a physics-informed neural network framework, Expert Systems with Applications, 2025, 275: 127098.

[61] Ren J, Xiao L. Physics-guided neural network for fatigue life prediction of FCC-based multi-principal element alloys, Scripta Materialia, 2024, 253: 116307.

[62] Akbari E, Tajbakhsh NC, Tabrizchi H, Mosavi A. Physics-informed neural networks for multiaxial fatigue life prediction of aluminum alloy, Computer Modeling in Engineering and Sciences, 2025, 145(1): 305.

[63] Editorial Board of Material Data Sheet of Aircraft Engine Design. Material manual for aero engine design, Aviation Industry Press, 2010.

[64] Academic Committee of the Superalloys. China superalloys handbook, China Zhijian Publishing House and Standards Press of China, 2012.